



Enhanced visible light photoelectrocatalytic degradation of *o*-chloronitrobenzene through surface plasmonic Au nanoparticles and g-C₃N₄ co-modified TiO₂ nanotube arrays photoanode

Shuaishuai Xin^{a,c}, Xiaoming Ma^a, Jinren Lu^b, Guangshan Zhang^c, Siyue Huo^a, Mengchun Gao^{a,*}, Peng Xu^d, Wenjie Liu^a, Wenxian Fu^a

^a Key Lab of Marine Environment and Ecology, Ministry of Education, Ocean University of China, Qingdao 266100, China

^b College of Chemistry & Chemical Engineering, Ocean University of China, Qingdao 266100, China

^c Qingdao Engineering Research Center for Rural Environment, College of Resources and Environment, Qingdao Agricultural University, Qingdao 266109, China

^d State Key Laboratory of Urban Water Resource and Environment, School of Environment, Harbin Institute of Technology, Harbin 150090, China

ARTICLE INFO

Keywords:

o-Chloronitrobenzene
Photoelectrocatalytic degradation
TiO₂ nanotube arrays
Graphitic carbon nitride
Au nanoparticles

ABSTRACT

Chloronitrobenzenes are typical refractory aromatic halogenated nitroaromatic and high-toxic contaminants. The reduction process of chloronitrobenzenes cannot realize their mineralization, and the existence of chlorine group is detrimental to degradation through single chemical oxidation technology. Herein, the Au nanoparticles and graphitic carbon nitride co-modified TiO₂ nanotube arrays (Au/g-C₃N₄/TNAs) photoanodes were fabricated to degrade *o*-chloronitrobenzene (*o*-CNB) target pollutant in photoelectrocatalytic (PEC) system. The Au/g-C₃N₄/TNAs fabricated with 0.20 mM HAuCl₄·0.4 H₂O (Au/g-C₃N₄/TNAs-0.20) had more superior optical and photoelectrochemical properties than other fabricated photoanodes. Au/g-C₃N₄/TNAs-0.20 photoanode increased dechlorination efficiency through reduction process, which was beneficial to *o*-CNB degradation and TOC removal. The coexistence of anions and humic acid inhibited the PEC degradation of *o*-CNB. The photogenerated electron, •O₂⁻, hole and •OH participated in *o*-CNB degradation in PEC system. The degradation pathway of *o*-CNB was inferred through GC-MS spectra and DFT calculation. The acute toxicity and bioaccumulation factor of *o*-CNB were effectively reduced by PEC degradation.

1. Introduction

Chloronitrobenzenes, typical halogenated nitroaromatic and high-toxic compounds, have been frequently detected in aquatic environment due to their extensive application in the production of pesticides, pharmaceuticals, dyes and corrosion inhibitors [1]. To eliminate the potential threat of residual chloronitrobenzene in water to the ecosystem, several techniques so far have been developed to remove chloronitrobenzene from water, such as biological treatment [2], adsorption [3] and heterogeneous reduction [4]. The removal efficiency of chloronitrobenzenes by biological treatment is very low due to their high stability and recalcitrance to biodegradation. The adsorption and heterogeneous reduction cannot realize the mineralization of chloronitrobenzenes fundamentally. The chlorine group on benzene ring of chloronitrobenzenes have strong electron-withdrawing, which may consume plenty of chemicals and energy through single chemical

oxidation technology for chloronitrobenzene degradation [5]. Previous studies have demonstrated that the reduction combined with oxidation process (e.g., Fe⁰-Fenton [6], Fe⁰-Persulfate [7] and GAC-Fe⁰-Cu⁰ micro-electrolysis [8] systems) can degrade chloronitrobenzene pollutants quickly after the removal of chlorine group by reduction process. However, the application of zero valent metals was limited in long-term operation processes due to their secondary pollution and poor stability. Therefore, it is necessary to develop a green and effective sustainable reduction combined with oxidation technique for chloronitrobenzene degradation.

The photoelectrocatalytic (PEC) technology, a combination of photocatalysis (PC) and electrocatalysis (EC), has received extensive attention for environmental remediation since it can achieve simultaneous reduction and oxidation reactions [9]. In a typical PEC system under light irradiation, electrons are excited from the valence band (VB) of photoanode into the conduction band (CB) and can quickly transfer to

* Corresponding author.

E-mail address: mengchungao@outlook.com (M. Gao).

<https://doi.org/10.1016/j.apcatb.2022.122174>

Received 19 June 2022; Received in revised form 27 October 2022; Accepted 10 November 2022

Available online 12 November 2022

0926-3373/© 2022 Elsevier B.V. All rights reserved.

the cathode by applying the anodic bias voltage, which can efficiently prevent the photogenerated carrier recombination and thereby increase the electron-hole pairs lifetime [10]. The photogenerated electrons and holes can participate in the reduction reaction on the cathode-electrolyte and the oxidation reaction on the photoanode-electrolyte interface, respectively. The PEC technology has been proved to be more efficient than PC or EC alone in the reduction dehalogenation and oxidation of refractory organic pollutants [11–14]. In recent years, numerous semiconductor materials have been served as photoanode in PEC for elimination of pollutants, such as TiO_2 , WO_3 , ZnO and BiVO_4 [10,15–18]. Among different photoanodes, TiO_2 nanotube arrays (TNAs) grown on the Ti sheet can be used not only as photocatalyst but also as electrode, and draw more attentions due to stable chemical properties, superior photoelectric conversion and controllability [11]. Compared with other photoanodes, the highly ordered and hollow tubular structure of TNAs can provide more photogenerated carrier transmission channels, thus accelerating the separation efficiency [19]. Nevertheless, the catalytic efficiency of TNAs photoanode under visible light irradiation is still limited by its easy photogenerated carrier recombination and low visible light utilization, critically hampering the potential application of TNAs photoanode in PEC degradation of organic pollutants.

Coupling TNAs with other matched narrow bandgap semiconductors to construct heterojunction has been considered as an effective method for the improvement of PEC performance by promoting visible light response and photogenerated carrier separation. Owing to the high chemical stability, superior electronic band structure and non-toxicity, the graphitic carbon nitride ($\text{g-C}_3\text{N}_4$) has been often employed to improve the visible light catalytic performance of TiO_2 in organic pollutants degradation [20], CO_2 reduction [21], H_2 evolution [22] and overall water splitting [23]. In addition, the photogenerated electrons exhibited great potential for dechlorination by reduction reactions due to the sufficient negative potential on CB position of $\text{g-C}_3\text{N}_4$ [19,24]. Previous research confirmed that the modification of TNAs photoanode by $\text{g-C}_3\text{N}_4$ ($\text{g-C}_3\text{N}_4/\text{TNAs}$) could accelerate the degradation of *p*-chloronitrobenzene compared to bare TNAs photoanode under visible light, which can be attributed to the well visible light response and high redox potentials of electron/hole of $\text{g-C}_3\text{N}_4/\text{TNAs}$ photoanode [19]. However, the large resistance of $\text{g-C}_3\text{N}_4$ blocks the transfer of photogenerated electrons [25], which was unfavorable for the degradation of organic pollutants by $\text{g-C}_3\text{N}_4/\text{TNAs}$ photoanode.

The surface plasmonic Au nanoparticles have currently gained much attention to improve the PEC performance of semiconductor photoanodes due to their strong surface plasmon resonance (SPR) effect in visible light region and effective ability to capture electrons [26–28]. For instance, Sun et al. reported that the PEC activities of CuI for oxidation of ethanol and organic contaminants could be enhanced by introducing Au nanoparticles under visible light [29]. Yin et al. demonstrated that the PEC performance of $\text{ZnSe}/\text{Au}/\text{TNAs}$ plasmonic photoelectrocatalyst could be improved due to the SPR effect of Au and the inhibition of photogenerated carrier recombination [30]. Furthermore, recent researches have also confirmed that the surface plasmonic Au nanoparticles could significantly improve the catalytic activity of powdered $\text{g-C}_3\text{N}_4/\text{TiO}_2$ photocatalyst in CO_2 reduction and hydrogen production by promoting the absorb efficiency of visible light and the separation efficiency of photogenerated carrier [31,32]. However, it is still unclear until now whether Au nanoparticles can improve the visible light PEC performance of $\text{g-C}_3\text{N}_4/\text{TNAs}$ photoanode in chloronitrobenzenes degradation.

Herein, a series of novel surface plasmonic Au nanoparticles and $\text{g-C}_3\text{N}_4$ co-modified TNAs ($\text{Au}/\text{g-C}_3\text{N}_4/\text{TNAs}$) photoanodes were fabricated by a facile three-step procedure (Fig. S1) and systematically analyzed through multiple characterizations. The PEC performance of fabricated photoanodes was evaluated through the degradation of *o*-chloronitrobenzene (*o*-CNB) target pollutant under visible light. The effects of main parameters on PEC degradation of *o*-CNB were

investigated, such as bias voltages, solution pH, inorganic anions and humic acid. The quenching experiments and electron spin resonance (ESR) spectra were carried out for identifying the major reactive species for the degradation of *o*-CNB. Degradation pathway of *o*-CNB was proposed according to gas chromatography mass spectrometry (GC-MS) and density functional theory (DFT) calculation. The toxicities of *o*-CNB and its degradation products were assessed through Toxicity Estimation Software Tool.

2. Experimental

2.1. Photoanodes fabrication and characterization

All chemical reagents were purchased from commercial sources and used without further purification for all experiments. The fabrication details of TNAs and $\text{g-C}_3\text{N}_4/\text{TNAs}$ photoanodes were provided in Text S1. The $\text{Au}/\text{g-C}_3\text{N}_4/\text{TNAs}$ photoanodes were fabricated by the Au reduction and chemical bath deposition processes. Firstly, excessive trisodium citrate was added the 100 mL different concentrations of $\text{HAuCl}_4 \cdot 0.4 \text{ H}_2\text{O}$ solution and stirred vigorously at 100°C until the reaction solution changed from yellow to red wine color. Secondly, the as-fabricated $\text{g-C}_3\text{N}_4/\text{TNAs}$ photoanodes were immersed into the above solution for 40 min to deposit Au nanoparticles on $\text{g-C}_3\text{N}_4/\text{TNAs}$ photoanodes surface. Finally, $\text{Au}/\text{g-C}_3\text{N}_4/\text{TNAs}$ photoanodes were obtained by annealing the deposited photoanode in muffle furnace at 200°C for 1 h. The concentrations of $\text{HAuCl}_4 \cdot 0.4 \text{ H}_2\text{O}$ used in the Au reduction process were 0.10, 0.15, 0.20, 0.25 and 0.30 mM, and the corresponding $\text{Au}/\text{g-C}_3\text{N}_4/\text{TNAs}$ photoanodes were marked as $\text{Au}/\text{g-C}_3\text{N}_4/\text{TNAs}$ -0.10, $\text{Au}/\text{g-C}_3\text{N}_4/\text{TNAs}$ -0.15, $\text{Au}/\text{g-C}_3\text{N}_4/\text{TNAs}$ -0.20, $\text{Au}/\text{g-C}_3\text{N}_4/\text{TNAs}$ -0.25 and $\text{Au}/\text{g-C}_3\text{N}_4/\text{TNAs}$ -0.30, respectively. The crystalline structure, surface morphology, chemical composition, optical and photoelectrochemical properties of the fabricated photoanodes were characterized in detail (Text S2).

2.2. PEC degradation of *o*-CNB

The degradation experiments were performed under visible light to estimate the PEC performances of photoanodes in a cylindrical quartz reactor containing 50 mL *o*-CNB (0.18 mM) and Na_2SO_4 (0.10 M) solution. The visible light source and bias voltage were supported by a xenon lamp with an ultraviolet cut-off filter ($\lambda > 420 \text{ nm}$) and a direct-current power supply, respectively. The distance between the visible light sources and the photoanodes was fixed at 2 cm. Prior to the PEC degradation experiments, the *o*-CNB solution was stirred for 60 min in dark to obtain the adsorption-desorption equilibrium between photoanodes and *o*-CNB. Afterwards, the PEC degradation experiments were started by turning on the light source and power supply. At regular intervals of reaction, a certain amount of *o*-CNB solution was taken out with a syringe for analysis. *o*-CNB concentrations were determined at 260 nm using a UV-Vis spectrophotometer (UV-6000, METASH). Active radicals were determined by an ESR spectrometer (Bruker EMX EPR) with 5,5-dimethyl-L-pyrroline N-oxide (DMPO) as capture agent. Degradation products of *o*-CNB were identified by the GC-MS and DFT calculation. GC-MS analysis and DFT calculation parameters were recorded in Text S3 and Text S4, respectively. The toxicities of *o*-CNB and its degradation products were assessed through Toxicity Estimation Software Tool.

3. Results and discussions

3.1. Crystalline structure

The X-ray diffraction (XRD) patterns and Raman spectra were analyzed to investigate crystalline structures of different photoanodes. The XRD patterns (Fig. 1a) confirmed that the crystal planes of anatase TiO_2 and rutile TiO_2 could be formed on Ti substrate through

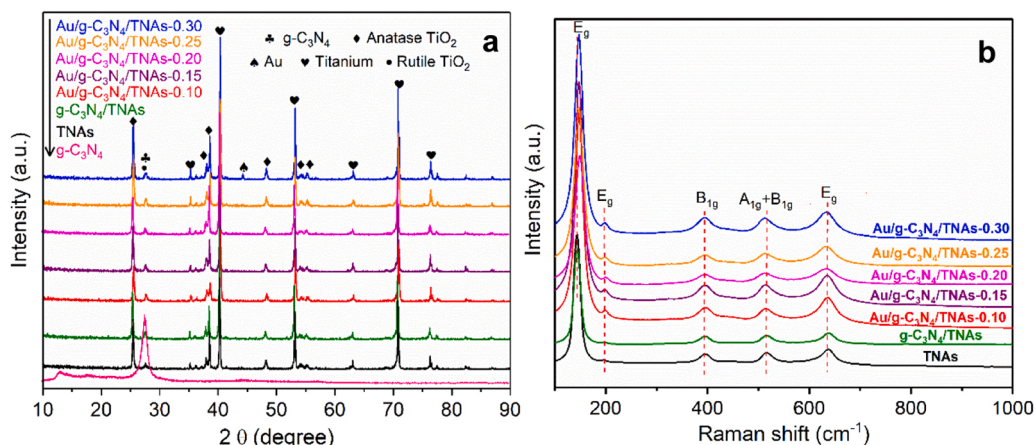


Fig. 1. XRD patterns (a) of g-C₃N₄ powder and various photoanodes, Raman spectra (b) of various photoanodes.

anodization [19,33]. For Au/g-C₃N₄/TNAs photoanodes, the intensity of diffraction peaks belonging to g-C₃N₄ at 27.6° was stronger than that of TNAs, and the Au/g-C₃N₄/TNAs-0.30 displayed diffraction peak belonging to Au at 44.3° [31]. The present results demonstrated that the g-C₃N₄ and Au were successfully attached to the TNAs. The XRD patterns of Au/g-C₃N₄/TNAs-0.10, Au/g-C₃N₄/TNAs-0.15, Au/g-C₃N₄/TNAs-0.20 and Au/g-C₃N₄/TNAs-0.25 displayed no the peaks belonging to Au, which may be attributed to low content and high dispersion of Au

particles on the g-C₃N₄/TNAs surface. Raman spectra (Fig. 1b) in 100–1000 cm⁻¹ range of different photoanodes exhibited five major peaks at around 144, 200, 396, 517 and 638 cm⁻¹ corresponding to E_g, E_g, B_{1g}, A_{1g}+B_{1g}, and E_g modes of anatase TiO₂, respectively. The E_g, B_{1g} and A_{1g} peaks were ascribed to the symmetric stretching vibrations, symmetric bending vibrations and anti-symmetric bending vibrations of O-Ti-O in anatase TiO₂, respectively [34]. Note that the E_g peak of Au/g-C₃N₄/TNAs photoanodes shifted to higher wave number

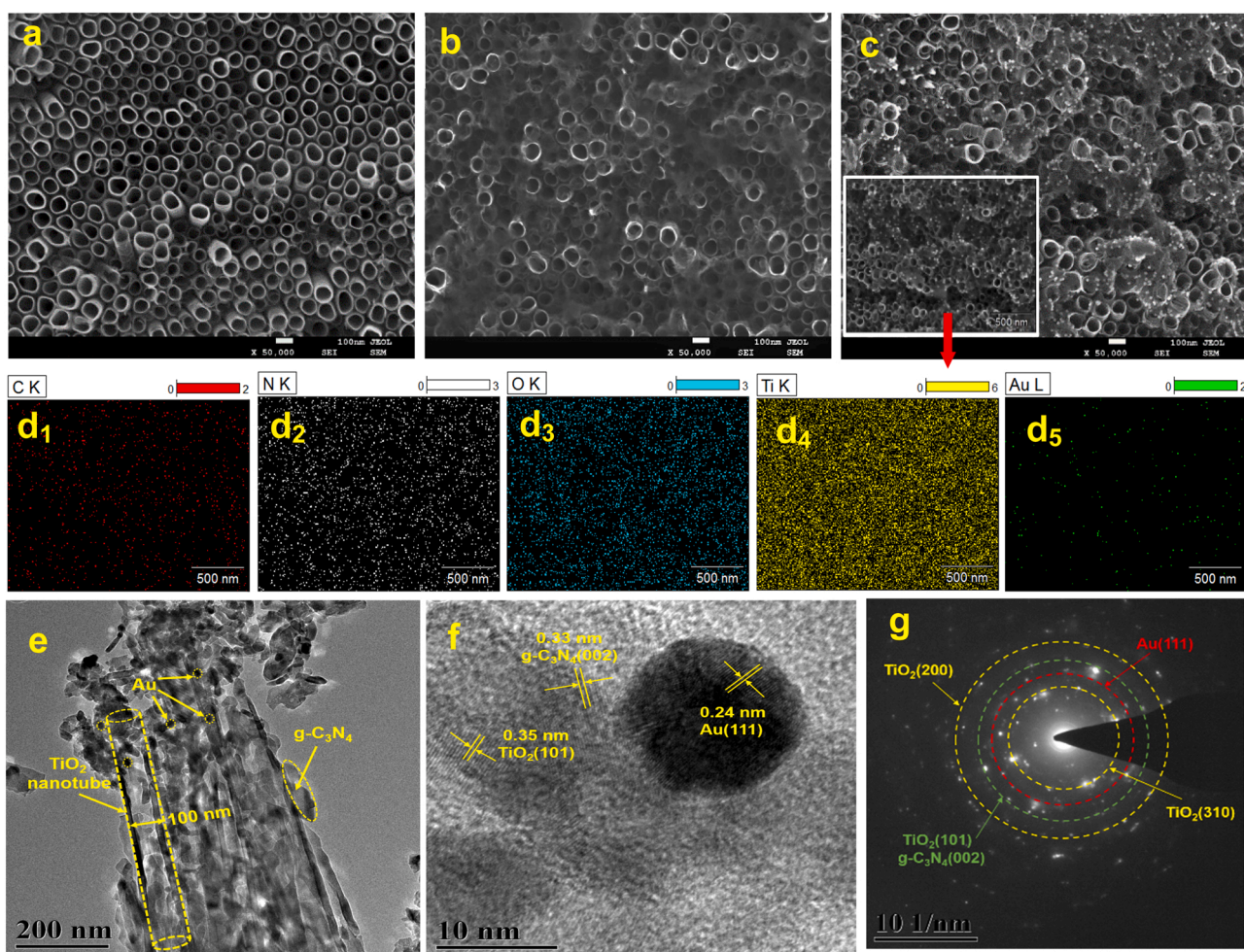


Fig. 2. SEM images of TNAs (a), g-C₃N₄/TNAs (b) and Au/g-C₃N₄/TNAs-0.20 (c). Elemental mapping of the inset in SEM image of Au/g-C₃N₄/TNAs-0.20: (d1-d5) correspond to C, N, O, Ti and Au maps, respectively. TEM (e), HRTEM (f) image and SAED pattern (g) of Au/g-C₃N₄/TNAs-0.20.

compared with g-C₃N₄/TNAs and TNAs, suggesting that the Au loading could increase crystal defects in TiO₂ and act as photoelectrons capture position [35]. Nevertheless, the peaks related to g-C₃N₄ and rutile TiO₂ were not detected at Raman spectra of g-C₃N₄/TNAs and Au/g-C₃N₄/TNAs, which may be due to the strong fluorescence property of g-C₃N₄ and low content of rutile TiO₂ [36]. In addition, Raman spectrum is generally molecular spectra, thus Ti metal has no peaks at Raman spectra of g-C₃N₄/TNAs and Au/g-C₃N₄/TNAs due to its atomic structure.

3.2. Surface morphology and elemental composition

As shown in the scanning electron microscopy (SEM) image of TNAs (Fig. 2a), the TiO₂ nanotubes in the bare TNAs were highly ordered and

vertically oriented on the titanium substrate without any impurities. The average inner diameter and wall thickness of TiO₂ nanotubes were about 100 nm and 15 nm, respectively. For g-C₃N₄/TNAs photoanode, g-C₃N₄ was evenly deposited on TiO₂ nanotubes surface after TNAs was soaked in melamine ethylene glycol solution and then annealed at 550 °C (Fig. 2b). Figs. 2c and S2 revealed that Au nanoparticles with average diameter of 7 nm were highly dispersed on Au/g-C₃N₄/TNAs-1.0, Au/g-C₃N₄/TNAs-1.5, Au/g-C₃N₄/TNAs-2.0 and Au/g-C₃N₄/TNAs-2.5 photoanodes surface, whereas Au/g-C₃N₄/TNAs-3.0 surface was covered by Au nanoparticles with large particles. The above phenomena can be explained that the load content of Au nanoparticles on Au/g-C₃N₄/TNAs photoanodes surface increased with the concentrations of HAuCl₄·0.4 H₂O from 0.10 to 0.30 mM during the Au reduction process (Fig. S3 and Table S1). The agglomeration of Au nanoparticles on Au/g-

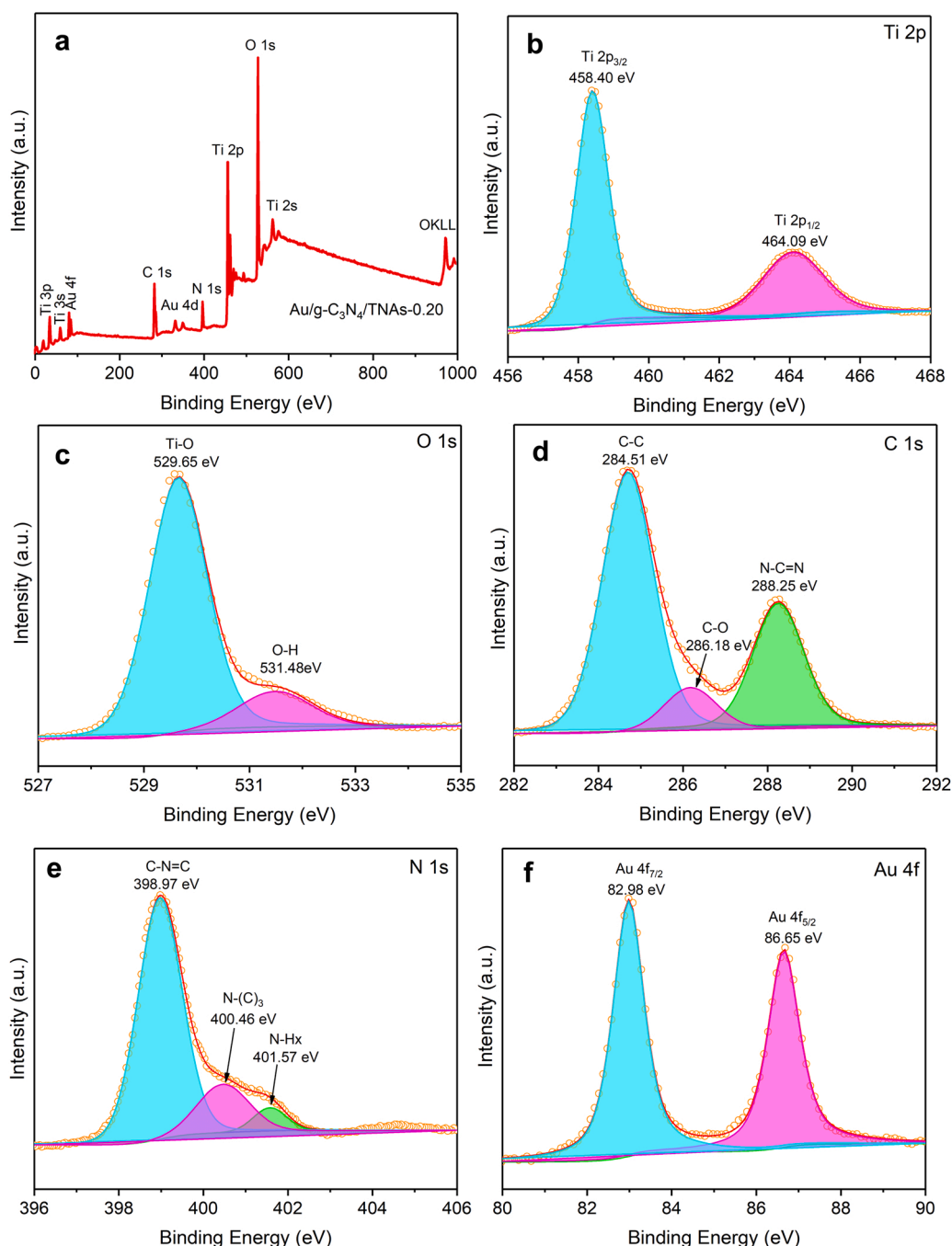


Fig. 3. The full survey XPS spectrum (a), high-resolution Ti 2p (b), O 1s (c), C 1s (d), N 1s (e) and Au 4f (f) of Au/g-C₃N₄/TNAs-0.20.

C₃N₄/TNAs-3.0 surface could cause the variation of Au crystalline structures on the g-C₃N₄/TNAs photoanode, which can be supported by the results of XRD patterns. Compared with Au/g-C₃N₄/TNAs-0.20, less Au nanoparticles were attached to Au/g-C₃N₄/TNAs-0.10 and Au/g-C₃N₄/TNAs-0.15 surfaces (Fig. S2a and b), while the higher Au nanoparticles load content in Au/g-C₃N₄/TNAs-x (x = 0.25 and 0.30) led to the agglomeration of Au nanoparticles and blocked the nanotube orifice (Fig. S2c and d). The EDS spectra (Fig. S3) and elemental maps (Fig. 2d) showed the coexistence and distribution of C, N, O, Ti and Au on Au/g-C₃N₄/TNAs-0.20 surface, which further suggested that g-C₃N₄ and Au nanoparticles were successfully attached to TNAs surface. Moreover, the ultra-structure of crystal lattice of Au/g-C₃N₄/TNAs-0.20 was observed in the transmission electron microscope (TEM), high-resolution TEM (HRTEM) and selected area electron diffraction (SAED). The Au nanoparticles and g-C₃N₄ adhered to TiO₂ nanotubes with a diameter of 100 nm were observed from the TEM image of Au/g-C₃N₄/TNAs-0.20 (Fig. 2e). Fig. 2f showed that the lattice spacing of 0.24 nm, 0.33 nm and 0.35 nm in the HRTEM image of Au/g-C₃N₄/TNAs-0.20 matched with Bragg reflections from Au (111), g-C₃N₄ (002) and TiO₂ (101) planes, respectively. The SAED pattern displayed that the polycrystalline planes (e.g., TiO₂ (310), TiO₂ (101), TiO₂ (200), g-C₃N₄(002) and Au (111)) was formed on Au/g-C₃N₄/TNAs-0.20 photoanode (Fig. 2g), which further confirmed that g-C₃N₄ and Au was successfully loaded on TNAs. The full survey X-ray photoelectron spectroscopy (XPS) spectrum displayed that the Ti, O, C, N, and Au existed on Au/g-C₃N₄/TNAs-0.20 surface (Fig. 3a), which was consistent with EDS result. In the high-resolution Ti 2p spectrum (Fig. 3b), two peaks at 458.40 eV and 464.10 eV were assigned to the Ti 2p_{3/2} and Ti 2p_{1/2} in the present of Ti⁴⁺ state [31], implying that titanium sheet was oxidized to TiO₂ nanotubes through anodization. Fig. 3c showed that the high-resolution O 1s spectrum was deconvoluted into two peaks of 529.95 and 531.56 eV groups, which were corresponded to the Ti-O-C band at the interface between TiO₂ and

g-C₃N₄ and the surface -OH groups, respectively [31]. The high-resolution C 1s spectrum (Fig. 3d) were divided into three peaks of C-C (284.51 eV), C=N (286.18 eV) and C-N/C-(N)₃ (288.25 eV) groups. Three deconvoluted peaks at 398.97 eV, 400.46 eV and 401.57 eV corresponding to C-N=C, N-(C)₃ and N-H_x were observed in the high-resolution N 1s spectrum (Fig. 3e) [37]. The results of the high-resolution C 1s spectrum and N 1s spectrum demonstrated that g-C₃N₄ was attached to Au/g-C₃N₄/TNAs-0.20 surface. The binding energies at 82.98 eV and 86.65 eV in the high-resolution Au 4f spectrum were assigned to the Au 4f_{7/2} and Au 4f_{5/2} (Fig. 3f), suggesting that metallic Au nanoparticles were successfully attached to Au/g-C₃N₄/TNAs-0.20 [38].

3.3. Optical properties and band structure

The light absorption properties of photoanodes were evaluated through UV-Vis diffuse reflectance spectra. As depicted in Fig. 4a, the light absorption boundaries of TNAs, g-C₃N₄ and g-C₃N₄/TNAs were 388 nm, 475 nm and 431 nm, respectively, indicating that g-C₃N₄ had good visible light response and could improve visible light absorption activity of TNAs photoanode. Compared with g-C₃N₄/TNAs, the light absorption boundaries of Au/g-C₃N₄/TNAs-x (x = 0.10, 0.15, 0.20, 0.25 and 0.30) displayed a distinct red shift owing to the SPR effect of Au nanoparticles in visible light region [31]. Moreover, Au/g-C₃N₄/TNAs-0.20 existed more superior visible light response than other photoanodes with the maximum light absorption boundary at 440 nm. Based on the Kubelka-Munk function [19,33], the calculated bandgap energy (*E_g*) of TNAs, g-C₃N₄ powder and g-C₃N₄/TNAs were 3.09, 2.67 and 2.90 eV, respectively (Fig. 4b). Likewise, all Au/g-C₃N₄/TNAs photoanodes, especially Au/g-C₃N₄/TNAs-0.20 photoanode, displayed narrower bandgap than g-C₃N₄/TNAs and TNAs, which suggested that g-C₃N₄ and Au nanoparticles could effectively narrow the bandgap of

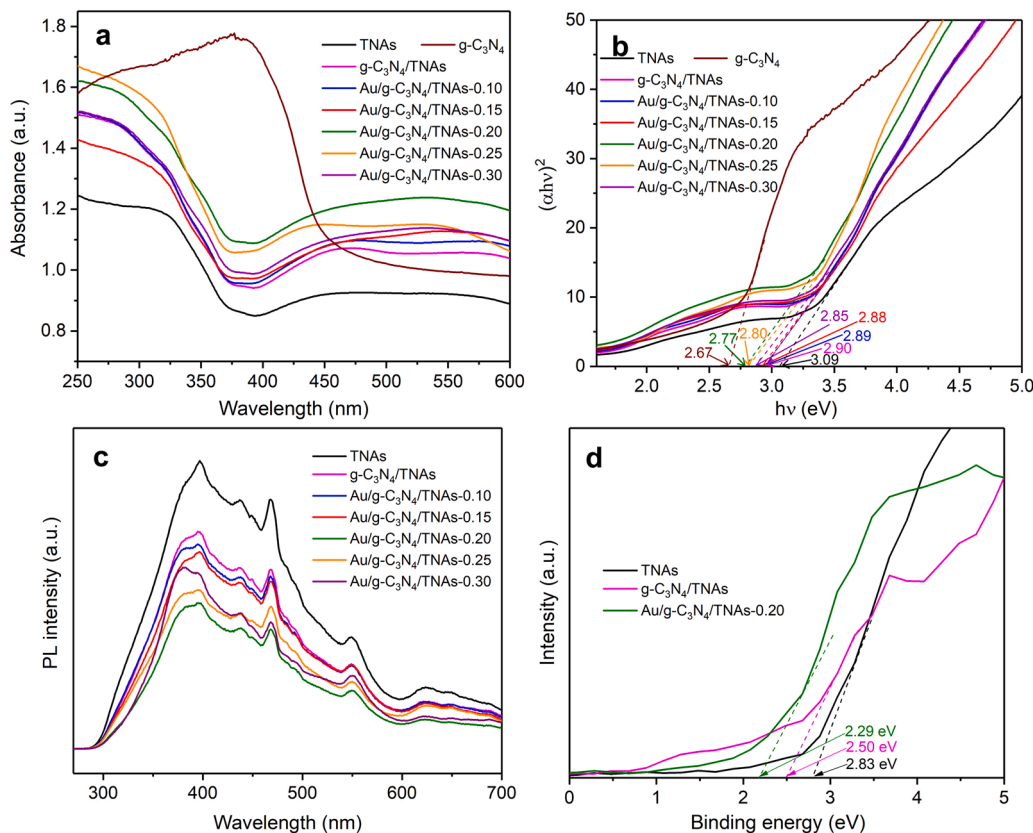


Fig. 4. UV-Vis diffuse reflectance spectra (a), $(\alpha h\nu)^2$ versus $h\nu$ plots (b) of g-C₃N₄ and different photoanodes, photoluminescence spectra (c) of different photoanodes, XPS valence band spectra (d) of TNAs, g-C₃N₄/TNAs and Au/g-C₃N₄/TNAs-0.20.

TNAs photoanode.

To estimate the effect of g-C₃N₄ and Au nanoparticles on the recombination efficiency of photogenerated carrier of TNAs, the steady state photoluminescence (PL) spectra of TNAs, g-C₃N₄/TNAs and different Au/g-C₃N₄/TNAs photoanodes were investigated under excitation at a wavelength of 260 nm within the wavelength range of 250–700 nm. As shown in Fig. 4c, the PL intensity of TNAs had the strongest emission peak due to the highest recombination efficiency of photogenerated carrier. Compared with TNAs, g-C₃N₄/TNAs photoanode exhibited weaker PL intensity, suggesting that g-C₃N₄ could reduce recombination efficiency of photogenerated carrier [24]. The PL intensities of all Au/g-C₃N₄/TNAs photoanodes were further decreased, indicating that the photogenerated carrier recombination was inhibited after the Au nanoparticles was attached to g-C₃N₄/TNAs photoanode due to their SPR effect [31]. Au/g-C₃N₄/TNAs-0.20 exhibited the lowest PL intensity, indicating that the best separation performance of photogenerated electrons and holes was obtained through optimizing loading Au nanoparticles content. The results of UV-Vis diffuse reflectance and

PL spectra confirmed that the SPR effect of loaded Au nanoparticles could improve light absorption property and inhibit photogenerated carrier recombination of photoanodes, which was beneficial for enhancing the photoelectrochemical performance compared with g-C₃N₄/TNAs photoanode.

The XPS-VB spectra were investigated to further clarify the influence of g-C₃N₄ and Au nanoparticles on band structure in TNAs photoanode (Fig. 4d). The VB energies of TNAs, g-C₃N₄/TNAs and Au/g-C₃N₄/TNAs-0.20 photoanodes were located at 2.83, 2.50 and 2.29 eV, respectively. Based on the result of $(ah\nu)^2$ versus $h\nu$ plots and XPS-VB spectra, the possible band structure was revealed and shown in Fig. S4. TNAs existed a bandgap energy of 3.09 eV between VB of 2.83 eV and CB of -0.26 eV. g-C₃N₄ loading on TNAs surface caused the formation of new VB (2.50 eV) and CB (-0.40 eV) in g-C₃N₄/TNAs, which led to a narrow bandgap energy of 2.90 eV. Au nanoparticles loading on g-C₃N₄/TNAs surface caused a narrower bandgap energy of 2.77 eV between VB of 2.29 eV and CB of -0.48 eV in Au/g-C₃N₄/TNAs-0.20, indicating that the SPR effect of loaded Au nanoparticles could cause up-shift of VB and

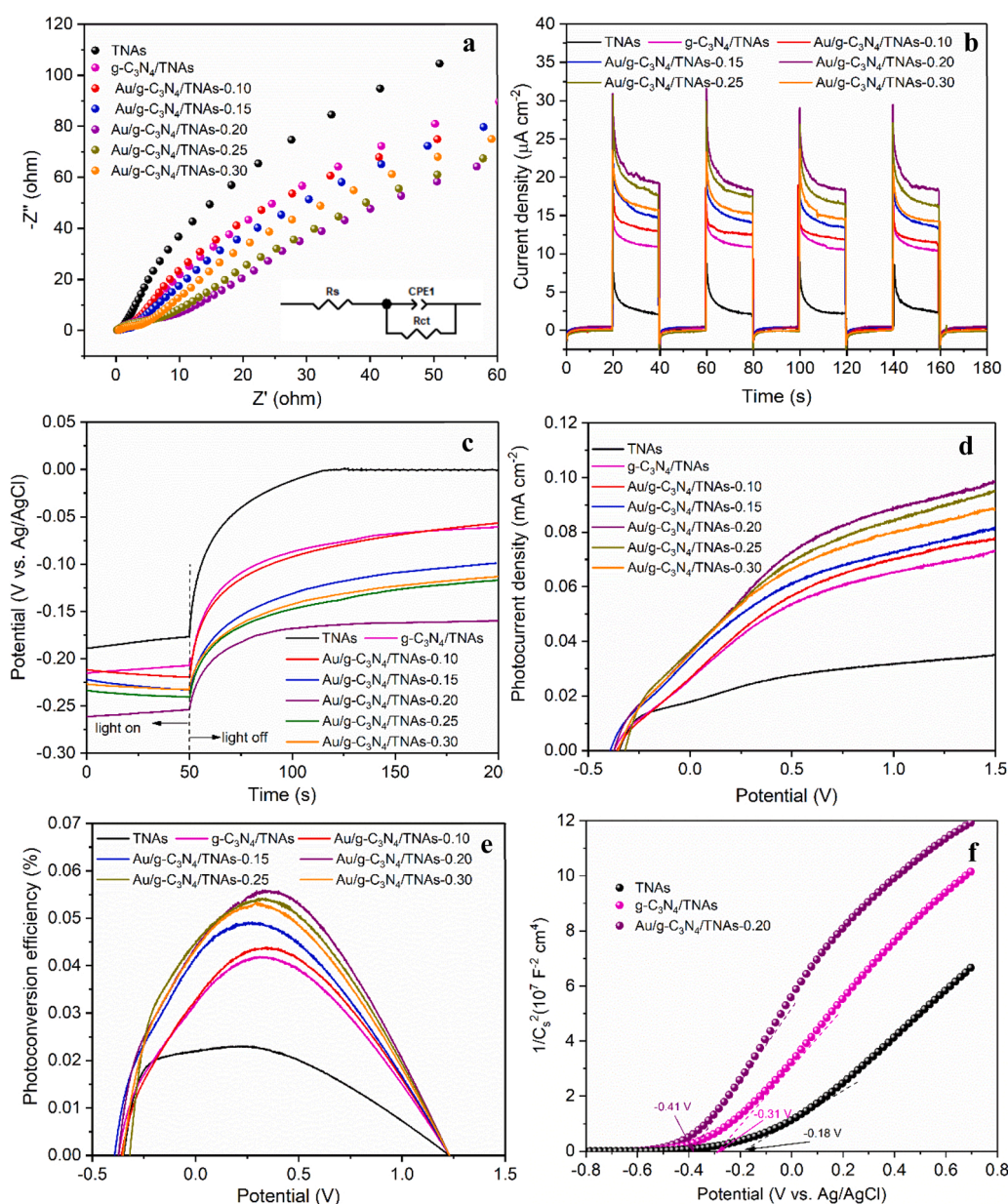


Fig. 5. EIS Nyquist plots (a), photocurrent response (b), open-circuit potential decay curves (c), LSV curves (d) and corresponding photoconversion efficiencies (e) of various photoanodes. Mott-Schottky curves (f) of TNAs, g-C₃N₄/TNAs and Au/g-C₃N₄/TNAs photoanodes.

CB [39].

3.4. Photoelectrochemical properties

To investigate the interior resistance and photogenerated carrier transfer kinetics of photoanodes, the electrochemical impedance spectrum (EIS) Nyquist plots (Fig. 5a) and photocurrent response (Fig. 5b) were performed under visible light. The electron transfer resistance can be represented through the semicircle in EIS Nyquist plots, and the smaller semicircles generally indicate lowest interfacial electron transfer resistance [40]. An equivalent circuit was proposed to explain the Nyquist plot (inset of Fig. 5a), and the fitted values of electrochemical parameters were summarized in Table S2. The g-C₃N₄ and Au nanoparticles have a slight effect on the electrolyte solution (R_s) of TNAs, whereas the charge transfer resistances (R_{ct}) of g-C₃N₄/TNAs and various Au/g-C₃N₄/TNAs photoanodes were significantly lower than that of TNAs. Notably, Au/g-C₃N₄/TNAs-0.20 photoanode possessed smallest semicircles and R_{ct} among fabricated photoanodes (Fig. 5a and Table S2), which accelerated the separation of photogenerated carrier. The photocurrent is formed mainly by transferring photoelectron to the counter electrode, and hence more effective separation and transport of photogenerated carrier implies higher photocurrent response [41]. As shown in Fig. 5b, TNAs produced a relatively low photocurrent density, whereas the photocurrent densities of g-C₃N₄/TNAs and Au/g-C₃N₄/TNAs increased significantly. Among fabricated photoanodes, Au/g-C₃N₄/TNAs-0.20 produced the highest photocurrent density, suggesting that the appropriate loading of g-C₃N₄ and Au nanoparticles could promote separation and transport of photogenerated carriers, and further improve photocatalytic activity. The open-circuit potential decay curves were analyzed to evaluate the lifetime of photoelectron in photoanodes. As displayed in Fig. 5c, all photoanodes possessed a stable open-circuit potential under continuous visible light, and the open-circuit potential of Au/g-C₃N₄/TNAs-0.20 was obviously higher than that of other photoanodes due to highest separation efficiency of photogenerated carriers, which is consistent with the result of photocurrent response. After the light off, the open-circuit potential decay rate of Au/g-C₃N₄/TNAs was significantly lower than those of g-C₃N₄/TNAs and TNAs. The photoelectron lifetime versus open-circuit voltage curves in Fig. S5 revealed that the Au/g-C₃N₄/TNAs-0.20 exhibited longer photoelectron lifetime than other photoanodes, indicating that the appropriate loading of Au nanoparticles could effectively inhibit photogenerated carrier recombination. The photoconversion efficiencies of photoanodes were investigated through linear sweep voltammetry (LSV) under the visible light. As illustrated in Fig. 5d, g-C₃N₄ and Au nanoparticles could obviously enhance the photocurrent density of TNAs, and Au/g-C₃N₄/TNAs-0.20 exhibited highest photocurrent density among fabricated photoanodes. The photoconversion efficiencies of photoanodes were calculated based on the LSV curve [42], and g-C₃N₄/TNAs and Au/g-C₃N₄/TNAs photoanodes had higher photoconversion efficiency than TNAs (Fig. 5e). Au/g-C₃N₄/TNAs-0.20 photoanode existed the maximum photoconversion efficiency (0.055%) among fabricated photoanodes, which was 2.39 times as high as that of TNAs (0.023%). The present results indicated that g-C₃N₄ and Au nanoparticles on TNAs surface could improve photogenerated carrier separation, photoelectron lifetime and photoconversion efficiency, which was beneficial for improving the photocatalytic performance.

The flat-band potential and photogenerated carrier density were evaluated from the Mott-Schottky curves (Fig. 5f) through the following formulas:

$$1/C_s^2 = \pm (2/e\epsilon\epsilon_0 N_A)(V - V_{fb} - KT/e) \quad (1)$$

$$N_A = (2/e\epsilon\epsilon_0)/[d(1/C_s^2)/dV]^{-1} \quad (2)$$

where C_s is space charge layer capacitance, e is elemental charge, ϵ is dielectric constant, ϵ_0 is permittivity of vacuum, N_A is majority carrier

density, V and V_{fb} are the applied potential and flat-band potential, respectively, KT/e is a temperature dependent correction term. The positive tangent slope in Mott-Schottky curves of TNAs, g-C₃N₄/TNAs and Au/g-C₃N₄/TNAs-0.20 photoanodes indicated that they exhibited n-type semiconductor behavior and the majority photogenerated carriers were electrons [43]. The flat-band potential can be acquired from the intercept of the line with $1/C_s^2 = 0$. Compared with TNAs (−0.18 V vs. Ag/AgCl), the flat-band potentials in g-C₃N₄/TNAs and Au/g-C₃N₄/TNAs-0.20 shifted to more negative flat-band potentials of −0.31 V vs. Ag/AgCl and −0.41 V vs. Ag/AgCl. The normal hydrogen electrode (NHE) potential is 0.197 V higher than the Ag/AgCl potential [44], thus the flat-band potentials of TNAs, g-C₃N₄/TNAs and Au/g-C₃N₄/TNAs-0.20 were converted to 0.017 V vs. NHE, −0.113 V vs. NHE and −0.213 V vs. NHE, respectively. The more negative flat-band potential indicated that Au/g-C₃N₄/TNAs-0.20 had more efficient photogenerated carrier separation [45], which is consistent with the result of EIS Nyquist plots. Additionally, the CB potential of n-type semiconductors is more negative by about −0.1 V to −0.3 V than the flat-band potential (vs. NHE) [46]. The CB potential of TNAs, g-C₃N₄/TNAs and Au/g-C₃N₄/TNAs-0.20 were −0.083 to −0.283 V vs. NHE, −0.213 to −0.413 V vs. NHE and −0.213 to −0.413 V vs. NHE, respectively. The CB positions of photoanodes calculated based on XPS-VB and UV-Vis diffuse reflectance spectra were close to the CB potentials acquired through Mott-Schottky curves, which further indicated that g-C₃N₄ and Au nanoparticles could cause CB position up-shift of TNAs photoanode. Based on the Eq. (5), the photogenerated carrier densities of TNAs, g-C₃N₄/TNAs and Au/g-C₃N₄/TNAs-0.20 were calculated to 5.63×10^{19} , 1.02×10^{20} and $7.12 \times 10^{20} \text{ cm}^{-3}$, respectively. The higher photogenerated carrier density in Au/g-C₃N₄/TNAs-0.20 is benefited to improve photocatalytic performance.

3.5. PEC performance for the degradation of o-CNB

3.5.1. Degradation of o-CNB in various systems

The catalytic performance of fabricated photoanodes for the degradation of o-CNB was estimated in various systems. Prior to all degradation experiments, the o-CNB solution was stirred for 60 min in dark to obtain the adsorption-desorption equilibrium between photoanodes and o-CNB. The adsorption removal efficiency of o-CNB by different photoanodes had no significant difference (Fig. S6), which suggested that the loading of g-C₃N₄ and Au nanoparticles would not affect the adsorption capacity of TNAs for o-CNB. The photolysis removal efficiency of o-CNB was only 17.9% under visible light after 300 min due to its high stability (Fig. 6a). Compared with the photolysis system, the degradation efficiency of o-CNB by TNAs increased by 7.3% in PC system, whereas g-C₃N₄/TNAs and Au/g-C₃N₄/TNAs-x (x = 0.10, 0.15, 0.20, 0.25 and 0.30) displayed an obvious increase for the degradation of o-CNB under visible light (Fig. S6). The degradation efficiency of o-CNB by Au/g-C₃N₄/TNAs-0.20 among fabricated photoanodes was highest and reached 67.4% after 300 min in PC system (Figs. 6a and S6), which was ascribed to the better optical and photoelectrochemical properties of Au/g-C₃N₄/TNAs-0.20. The PEC degradation efficiency of o-CNB by Au/g-C₃N₄/TNAs-0.20 increased to 80.8% after applying 1.5 V bias voltage, which was also higher than those by other photoanodes (Figs. 6a and S7). For comparison, the EC degradation of o-CNB by Au/g-C₃N₄/TNAs-0.20 was only 10.8% under 1.5 V bias voltage in the absence of visible light. To further investigate the PEC performance of Au/g-C₃N₄/TNAs-0.20, the apparent rate constants for the degradation of o-CNB based on pseudo-first-order kinetics model (Eq. (S1)) were analyzed in various systems (Fig. S8). The apparent rate constants of Au/g-C₃N₄/TNAs-0.20 for the degradation of o-CNB in PC and EC systems were 0.00373 and 0.000330 min^{−1} respectively. However, the apparent rate constant of Au/g-C₃N₄/TNAs-0.20 in PEC system increased to 0.00543 min^{−1}, which was 1.52 and 4.02 times of g-C₃N₄/TNAs (0.00357 min^{−1}) and TNAs (0.00135 min^{−1}), respectively. The present results demonstrated

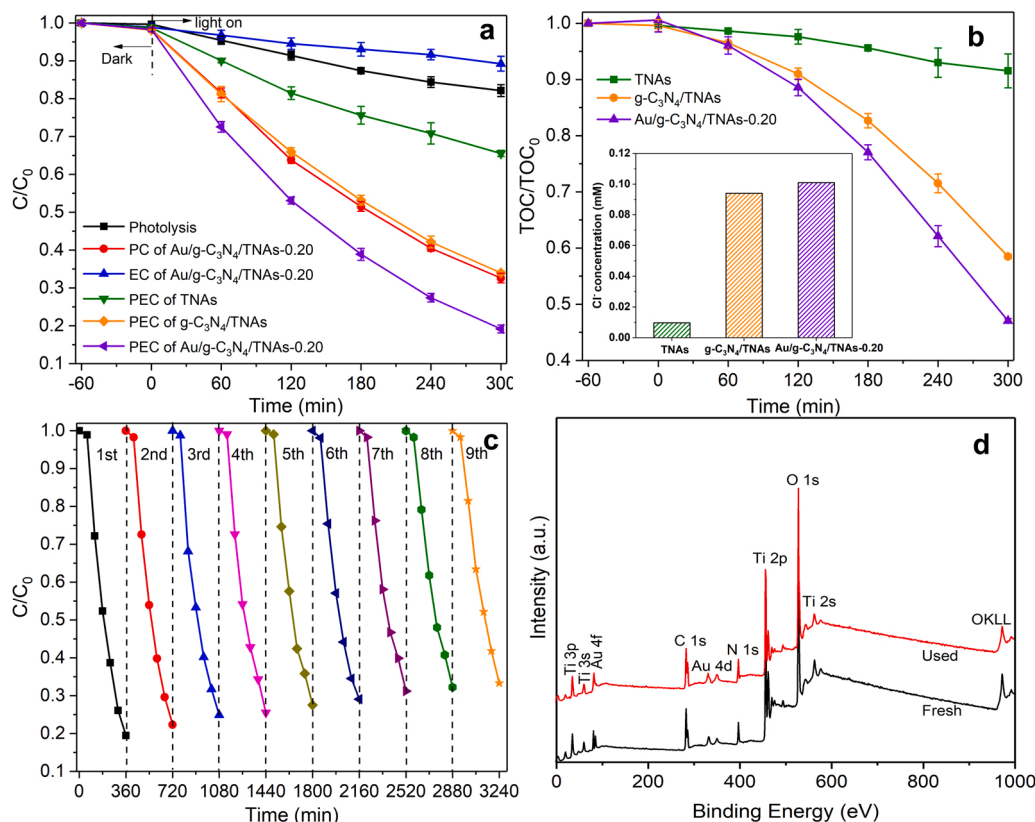


Fig. 6. Degradation (a) of *o*-CNB in various systems, TOC removal and Cl⁻ concentrations (the inset) in solution during the PEC degradation of *o*-CNB by TNAs, g-C₃N₄/TNAs and Au/g-C₃N₄/TNAs-0.20 (b), recycling degradation of *o*-CNB by Au/g-C₃N₄/TNAs-0.20 (c) and the full survey XPS spectra (d) of Au/g-C₃N₄/TNAs-0.20 before and after degradation in the PEC system ([*o*-CNB]₀ = 0.18 mM, pH = 7.0, bias voltage = 1.5 V and V = 50 mL).

that Au/g-C₃N₄/TNAs-0.20 was an effective photoanode for the degradation of *o*-CNB in PEC system, thus Au/g-C₃N₄/TNAs-0.20 was adopted as a typical photoanode to estimate its PEC performance for the degradation of *o*-CNB in the subsequent researches.

The total organic carbon (TOC) removal efficiency and Cl⁻ concentration in solution were determined to further estimate the PEC performance of different photoanodes for the degradation of *o*-CNB. As illustrated in Fig. 6b, the average TOC removal efficiency (53.0%) by Au/g-C₃N₄/TNAs-0.20 was higher than those by TNAs (41.5%) and g-C₃N₄/TNAs (8.47%) after 300 min in PEC system. Previous researches have confirmed that the removal of chlorine groups by reduction process could promote the degradation of chloronitrobenzene pollutants [6,7]. The inset in Fig. 6b showed that the degradation of *o*-CNB by TNAs, g-C₃N₄/TNAs and Au/g-C₃N₄/TNAs-0.20 photoanode could produce Cl⁻ with concentration of 0.01, 0.09 and 0.10 mM in solution, respectively. The present result suggested that the g-C₃N₄ and Au nanoparticles could improve dechlorination efficiency of *o*-CNB due to the more effective photogenerated carrier separation and longer photoelectron lifetime of Au/g-C₃N₄/TNAs-0.20, which further improve the PEC performance for *o*-CNB mineralization. Combined with the result in Fig. 6a, the PEC degradation efficiency of *o*-CNB by Au/g-C₃N₄/TNAs-0.20 was 80.8% after 300 min, indicating that *o*-CNB was not completely mineralized and approximately 27.8% *o*-CNB was transformed into degradation products.

The stability of Au/g-C₃N₄/TNAs-0.20 photoanode was investigated through nine consecutive recycling experiments for the degradation of *o*-CNB in PEC system. The degradation efficiency of *o*-CNB had no significant decrease and still remained approximately 70% after nine cycles (3240 min) in the PEC system (Fig. 6c). The full survey XPS spectra of Au/g-C₃N₄/TNAs-0.20 before and after nine consecutive recycling experiments still showed the existence of Ti, O, C, N, and Au (Fig. 6d),

which suggested that the g-C₃N₄ and Au nanoparticles on the TNAs surface were not destroyed during the degradation process. Although Cl⁻ could be detected in solution after the degradation of *o*-CNB, the full survey XPS spectra of used Au/g-C₃N₄/TNAs-0.20 had no any chlorine peak, which can be attributed to that the used Au/g-C₃N₄/TNAs-0.20 was washed using distilled water and dried prior to XPS detection, and the residual chlorine on the surface of Au/g-C₃N₄/TNAs-0.20 could be removed after simple washing. The present result demonstrated that Au/g-C₃N₄/TNAs-0.20 photoanode exhibited good stability for the degradation of *o*-CNB. Moreover, the leaching of Au was determined to be 0.008 mg in solution through inductively coupled plasma-atomic emission spectrometry after 300 min degradation, which might decrease degradation efficiency of *o*-CNB by Au/g-C₃N₄/TNAs-0.20 in PEC system.

3.5.2. Effects of bias voltages and solution pH on PEC degradation of *o*-CNB

The bias voltages could transfer photogenerated electrons on photoanode to the counter electrode and then affect the degradation of organic pollutants in PEC system [47]. Therefore, the effects of bias voltages on PEC degradation of *o*-CNB by Au/g-C₃N₄/TNAs-0.20 photoanode were investigated from 0.0 to 2.0 V. The degradation efficiency of *o*-CNB had an increasing trend with the increase of bias voltage, and the optimal degradation efficiency (80.8%) was obtained at 1.5 V after 300 min reaction (Fig. 7a). The apparent rate constant for the degradation of *o*-CNB at 1.5 V (0.00543 min⁻¹) enhanced 1.46, 1.37 and 1.14 times compared with those at 0.0 V (0.00373 min⁻¹), 0.5 V (0.00397 min⁻¹) and 1.0 V (0.00478 min⁻¹), respectively (Fig. S9a). The phenomenon can be attributed to the fact that the bias voltage promoted the photogenerated carriers separation and improved the PEC performance of Au/g-C₃N₄/TNAs-0.20 photoanode for the degradation

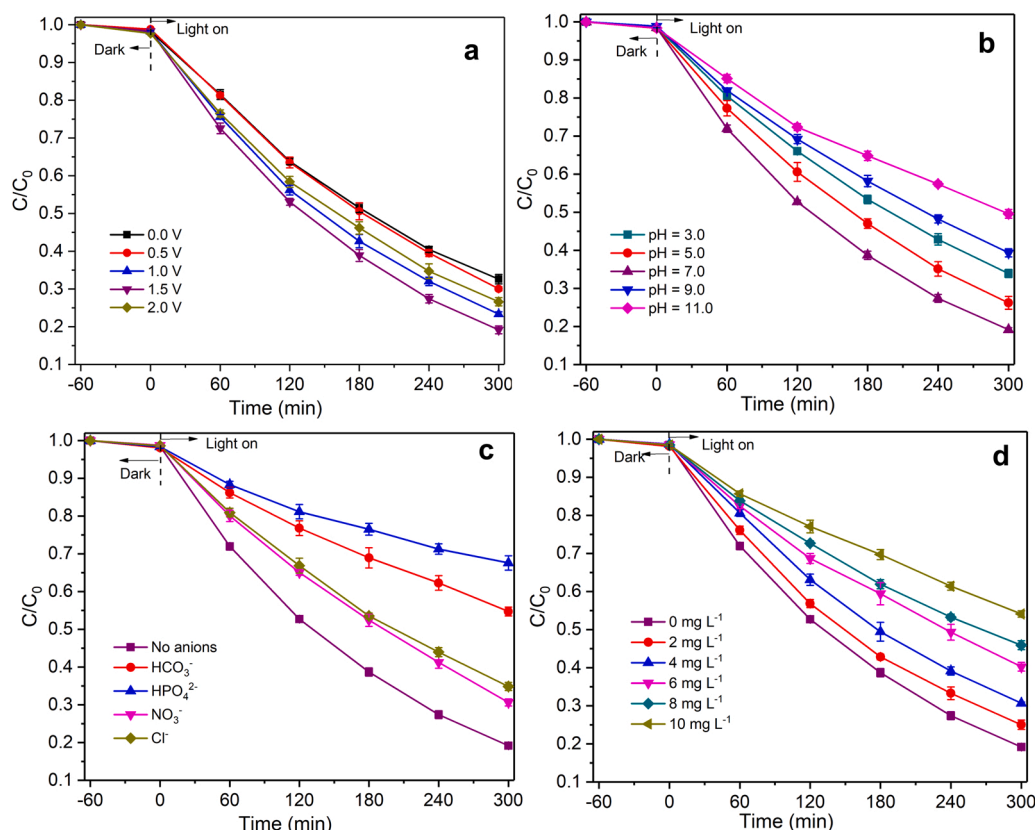


Fig. 7. Effects of bias voltages (a), solution pH (b), inorganic anions (c) and humic acid (d) on PEC degradation efficiency of *o*-CNB by Au/g-C₃N₄/TNAs-0.20 (Except for the investigated conditions, the others were fixed on [*o*-CNB]₀ = 0.18 mM, pH = 7.0, bias voltage = 1.5 V, V = 50 mL and [inorganic anions]₀ = 5 mM).

of *o*-CNB [11]. However, the degradation efficiency and apparent rate constant of *o*-CNB decrease to 73.4% and 0.00373 min⁻¹ with further increasing the bias voltage to 2.0 V, respectively. In general, the H₂O can be electrolyzed to form O₂ on photoanode surface at higher bias voltage, which was not conducive to light absorption and inhibited the PEC degradation of *o*-CNB [47].

The effects of solution pH with 3.0, 5.0, 7.0, 9.0 and 11.0 on degradation efficiency and apparent rate constant of *o*-CNB by Au/g-C₃N₄/TNAs-0.20 photoanode in PEC system were displayed in Figs. 7b and S9b. The degradation efficiency of *o*-CNB increased from 66.1% at pH 3.0–73.8% at pH 5.0% and 80.8% at pH 7.0, and the apparent rate constant increased from 0.00354 to 0.00543 min⁻¹ with solution pH from 3.0 to pH 7.0. However, degradation efficiency and apparent rate constant of *o*-CNB declined to 50.41% and 0.00225 min⁻¹ with increasing solution pH to 11.0. The adsorption removal efficiency of *o*-CNB by Au/g-C₃N₄/TNAs-0.20 had almost no change at various solution pH, which suggested that the solution pH would not affect the adsorption of *o*-CNB on Au/g-C₃N₄/TNAs-0.20 surface. The difference in degradation efficiency of *o*-CNB at various solution pH may be explained that the excess H⁺ at acidic conditions could capture photogenerated electrons and radical to form H₂O, whereas the HO⁻ at alkaline condition could capture radical and reduce the radical activity [44]. Similar result was also reported in degradation of *p*-CNB through g-C₃N₄/TNAs photoelectrode in PEC system [19].

3.5.3. Effects of inorganic anions and organic matters on PEC degradation of *o*-CNB

In practical water containing target pollutant, coexisting inorganic anions and natural organic matters may affect the degradation performance of photoanode in PEC system. Some common inorganic anions (e. g., NO₃⁻, Cl⁻, HCO₃⁻ and HPO₄²⁻) with the concentration of 5 mM were added during degradation process to investigate the effect of inorganic

anions on PEC degradation of *o*-CNB. Compared with the absence of anions, the presence of NO₃⁻ inhibited the PEC degradation of *o*-CNB (Figs. 7c and S9c). Although the NO₃⁻ cannot effectively quench HO[•] due to low reaction rate between HO[•] and NO₃⁻ [48], the NO₃⁻ could react with photogenerated electrons and holes to form NO₂⁻ and lower effective NO₃⁻, respectively (Eqs. (3) and (4)) [49]. The addition of Cl⁻ could capture photogenerated holes and HO[•] to form Cl[•] and Cl₂ (Eqs. (5) and (6)), which was unfavorable for the PEC degradation of *o*-CNB (Figs. 7c and S9c). In addition, Au particles (also Ti substrate) were very susceptible to chlorine radicals and could easily be poisoned, which could dampen the plasmonic activity and photoactivity. Moreover, the degradation of *o*-CNB could be inhibited when HCO₃⁻ and HPO₄²⁻ were added into the PEC system (Figs. 7c and S9c), which can be explained that HCO₃⁻ and HPO₄²⁻ was converted into lower effective HCO₃[•] and HPO₄^{•-} by photogenerated holes and HO[•] (Eqs. (7) and (8)). The present results demonstrated that the presence of inorganic anions could inhibit the PEC degradation of *o*-CNB and the inhibitory effects were shown as follows: HPO₄²⁻ > HCO₃⁻ > Cl⁻ > NO₃⁻.



Humic acid as a representative natural organic matter was selected to investigate the effect of organic matter on the PEC degradation of *o*-CNB

(Figs. 7d and S9d). The degradation efficiency and apparent rate constant of *o*-CNB decreased significantly from 80.8% and 0.00543 min^{-1} to 38.6% and 0.00195 min^{-1} with humic acid concentration from 0 to 10 mg L^{-1} , respectively. The inhibition of humic acid on PEC degradation of *o*-CNB could be explained that humic acid might occupy surface active sites and had an adverse effect on the light absorption of photoanode [50]. Meanwhile, humic acid competed with *o*-CNB and acted as the radical quencher, which caused undesirable radical consumption.

3.6. Reactive species and possible PEC mechanisms

3.6.1. Reactive species identification

The methyl alcohol (MeOH), *p*-benzoquinone (BQ), ethylene diamine tetra acetic disodium acid (EDTA-2Na) and AgNO_3 were selected to respectively investigate the contribution of $\cdot\text{OH}$, $\cdot\text{O}_2$, photogenerated holes and electrons for the degradation of *o*-CNB [44]. As shown in Figs. 8a and S10, the addition of different scavengers could inhibit the degradation of *o*-CNB compared with the control (no scavenger). The degradation efficiency and apparent rate constant of *o*-CNB reduced from 80.8% (0.00543 min^{-1}) of the control to 70.73% (0.00402 min^{-1}), 61.03% (0.00307 min^{-1}) and 58.13% (0.00280 min^{-1}) when the MeOH, EDTA-2Na and BQ were added into the PEC system, respectively. The present results indicated that the $\cdot\text{OH}$, $\cdot\text{O}_2$ and holes existed a practical effect on the degradation and mineralization of *o*-CNB due to their oxidative activity. In general, photogenerated electrons possessed reductive property and cannot degrade organic pollutants through oxidation process. Additionally, the PEC performance for organic pollutants degradation could be improved after capturing photogenerated electrons due to the inhibition of photo-generated carrier recombination [11]. However, the *o*-CNB degradation

and TOC removal efficiencies respectively decreased from 80.8% and 53.1% of the control to 49.7% and 28.0% when AgNO_3 as the scavenger of electrons was added into the PEC system in the present work (Figs. 8a and S11), which might be attributed to that the photogenerated electrons could remove chlorine groups by reduction process (Fig. 6b) and facilitate the degradation of *o*-CNB. The ESR/DMPO experiments were performed to clarify the active radical production in various systems. Fig. 8b and c showed that no signals were detected in the absence of light, whereas the peaks of $\text{DMPO}\cdot\text{O}_2^-$ with the intensity of 1:1:1:1 and $\text{DMPO}\cdot\text{OH}$ with the intensity of 1:2:2:1 were detected in PC and PEC systems, which demonstrated that $\cdot\text{OH}$ and $\cdot\text{O}_2$ could be produced by $\text{Au/g-C}_3\text{N}_4/\text{TNAs-0.20}$ under visible light. The peaks of $\text{DMPO}\cdot\text{O}_2^-$ and $\text{DMPO}\cdot\text{OH}$ in PEC system were more intense than those in PC system, indicating that the applied bias voltages could accelerate the $\cdot\text{OH}$ and $\cdot\text{O}_2$ production. Furthermore, the ESR spectrum of $\text{DMPO}\cdot\text{O}_2^-$ displayed more intense signal than that of $\text{DMPO}\cdot\text{OH}$ at the same reaction time in PEC system (Fig. 8d). The results of ESR/DMPO experiments demonstrated that the contribution of $\cdot\text{O}_2$ to *o*-CNB degradation was higher than that of $\cdot\text{OH}$ in PEC system.

3.6.2. Proposed mechanism

The possible mechanism for the degradation of *o*-CNB by $\text{Au/g-C}_3\text{N}_4/\text{TNAs-0.20}$ in PEC system was inferred based on the abovementioned results (Fig. 9). The CB potential of TiO_2 in TNAs and $\text{g-C}_3\text{N}_4$ was -0.26 and -1.07 eV , while the VB potential of TiO_2 and $\text{g-C}_3\text{N}_4$ was 2.83 and 1.60 eV , respectively. The $\text{g-C}_3\text{N}_4$ and Au nanoparticles loading on the TNAs surface caused the formation of new VB (2.29 eV) and CB (-0.48 eV) in $\text{Au/g-C}_3\text{N}_4/\text{TNAs-0.20}$, which led to a narrow bandgap energy of 2.77 eV (Fig. S4). Therefore, $\text{Au/g-C}_3\text{N}_4/\text{TNAs-0.20}$ photoanode could be excited to produce the hole and electron (Eq. (9)) under

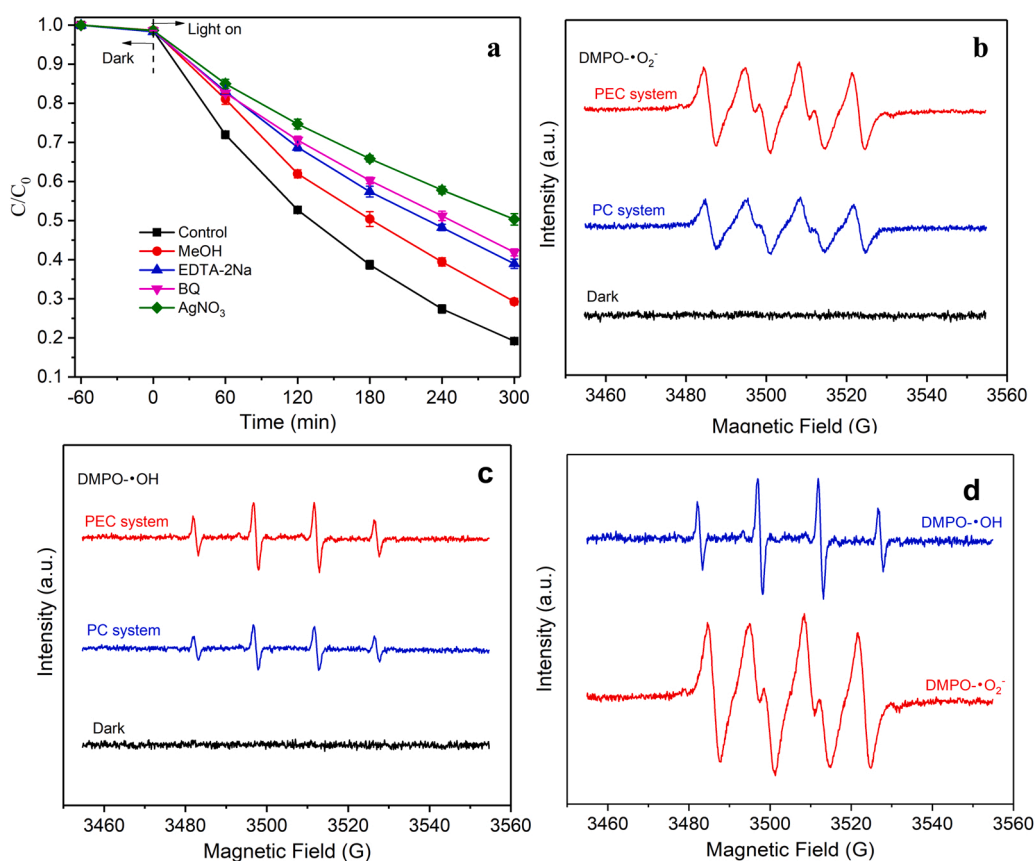


Fig. 8. Effects of different scavengers on *o*-CNB degradation (a) by $\text{Au/g-C}_3\text{N}_4/\text{TNAs-0.20}$ in PEC system, and ESR spectra of $\text{DMPO}\cdot\text{O}_2^-$ (b) and $\text{DMPO}\cdot\text{OH}$ (c) in various systems, and ESR spectra (d) of $\text{DMPO}\cdot\text{O}_2^-$ and $\text{DMPO}\cdot\text{OH}$ at the same reaction time in PEC system. ($[\text{o-CN}]\text{B}]_0 = 0.18 \text{ mM}$, $[\text{scavenger}]_0 = 5.0 \text{ mM}$, $\text{pH} = 7.0$, bias voltage = 1.5 V and $V = 50 \text{ mL}$).

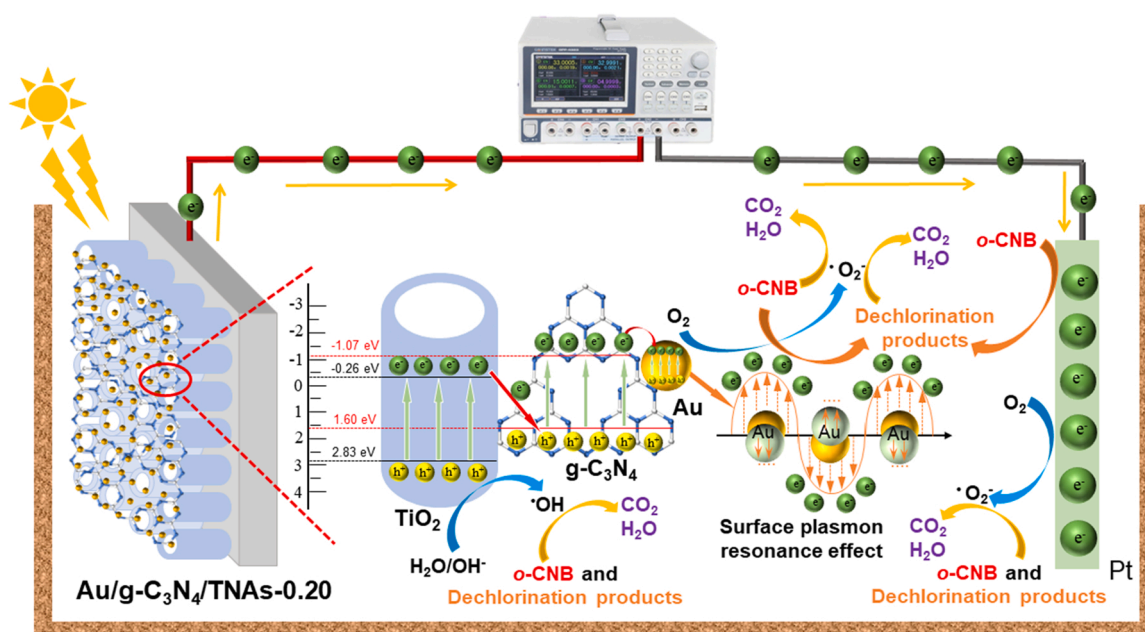
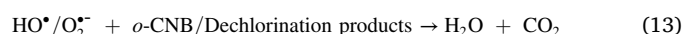
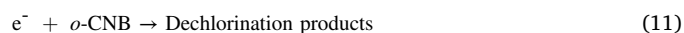
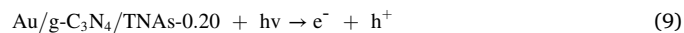


Fig. 9. Possible mechanism for *o*-CNB degradation by Au/g-C₃N₄/TNAs-0.20 in PEC system.

visible light. The photogenerated electrons on CB position of TNAs were easy to recombine with holes on VB position of g-C₃N₄ [19], which inhibited the photogenerated carrier recombination. The accumulated electrons on CB position of g-C₃N₄ were further transferred to Au nanoparticles, and the SPR effect of Au nanoparticles accelerated the electrons accumulation on the Au/g-C₃N₄/TNAs-0.20 photoanode surface. Due to the more negative CB potential of Au/g-C₃N₄/TNAs-0.20 than O₂/[•]O₂⁻ (-0.33 eV) [44], the photogenerated electrons could react with dissolved oxygen molecules to produce [•]O₂⁻ (Eq. (10)). The C-Cl bond in *o*-CNB could be attacked by the photogenerated electrons with strongly reductive activity through Eq. (11) to form dechlorination products and Cl⁻ in solution (Fig. 6b). In addition, the VB potential of TNAs was higher than •OH/H₂O (+2.68 eV) and •OH/OH⁻ (+1.99 eV) [51], thus the holes on VB position of TNAs could react with H₂O and OH⁻ to produce •OH (Eq. (12)). Meanwhile, the external electric field could provide a potential gradient, which derived partial photogenerated electrons along the external circuit to cathode at an appropriate bias voltage [52]. The transfer of photogenerated electrons could not only inhibit photogenerated carrier recombination of Au/g-C₃N₄/TNAs-0.20, but also promote the production of dechlorination products, •OH and •O₂⁻ through Eqs. (10)–(12). Subsequently, the produced radicals ([•]O₂⁻ and •OH) could further oxidize *o*-CNB and dechlorination products into CO₂ and H₂O (Eq. (13)).



3.7. Degradation products and toxicity estimation

To clarify the degradation pathway of *o*-CNB by Au/g-C₃N₄/TNAs-0.20 photoanode in PEC system, the GC-MS and DFT calculation were employed to identify the degradation products. The GC/MS spectra and the molecular structure diagrams of *o*-CNB as well as degradation products were displayed in Fig. S12. The peak at *m/z* of 157 was

designated as *o*-CNB, whereas the appearance of other peaks at *m/z* of 174, 125, 123, 111, 109, 95 and 93 indicated the generation of products during *o*-CNB degradation by Au/g-C₃N₄/TNAs-0.20 photoanode in PEC system. Furthermore, DFT calculation were adopted to predict the reaction sites and the bond breakage of *o*-CNB by radical attack (Fig. 10a and 10b). The atomic numbers in *o*-CNB chemical structure according to Fukui Function and Mulliken Population were shown in Fig. 10a. As shown in Fig. 10b, the larger *f*⁰ values of C 2, N 7, Cl 8, O 9 and O 10 atoms demonstrated that they were prone to radicals attack [53]. Similarly, the N 1 - O 1, N 1 - O 2, C 5 - N 1 and C 4 - Cl 1 bonds with smaller population values were more susceptible to be cleaved under radical attack [54]. According to the results of GC-MS and DFT calculation, the proposed degradation pathway of *o*-CNB was illustrated in Fig. 10c. The Cl 8 atom and C 4 - Cl 1 bond in *o*-CNB (*m/z* = 157) could be attacked by reactive species to produce P1 (*m/z* = 123) through dechlorination reaction. The N 7, O 9 and O 10 atoms in -NO₂ group with relatively large *f*⁰ values were more vulnerable to reactive species attack, resulting in the conversion of P1 to P2 (*m/z* = 93) through ammoniation reaction. The formed P2 was further transformed into P3 (*m/z* = 93) through the cleavage of C 5 - N 1 bond and hydroxylation reaction under •OH attack. Moreover, the formed P3 and *o*-CNB were converted into P7 (*m/z* = 111) and P4 (*m/z* = 174) through hydroxylation reaction on C 2 atom under •OH attack, respectively. P5 (*m/z* = 125) was generated from P4 by the cleavage of N 1 - O 1 and N 1 - O 2 bonds, which was further transformed into P6 (*m/z* = 109). P7 was also produced through deamination and hydroxylation reaction of P6. Subsequently, the formed degradation products were further mineralized to inorganic matter under reactive species attack.

The fathead minnow 50% lethal dose (LC₅₀-96 h) and bioaccumulation factor were used as indicators to estimate the toxicities of *o*-CNB and its degradation products after PEC degradation by Au/g-C₃N₄/TNAs-0.20 through the Toxicity Estimation Software Tool based on Quantitative Structure Activity Relationship prediction. The LC₅₀-96 h values of most degradation products except for P4 were higher than that of *o*-CNB (Fig. 11a), which suggested that the acute toxicity of *o*-CNB to fathead minnow was reduced in PEC system. Moreover, all degradation products existed lower bioaccumulation factor compared with *o*-CNB (Fig. 11b), suggesting that the degradation products were more difficult to accumulate in organisms than *o*-CNB. The results of toxicity prediction confirmed the overall toxicity of *o*-CNB was

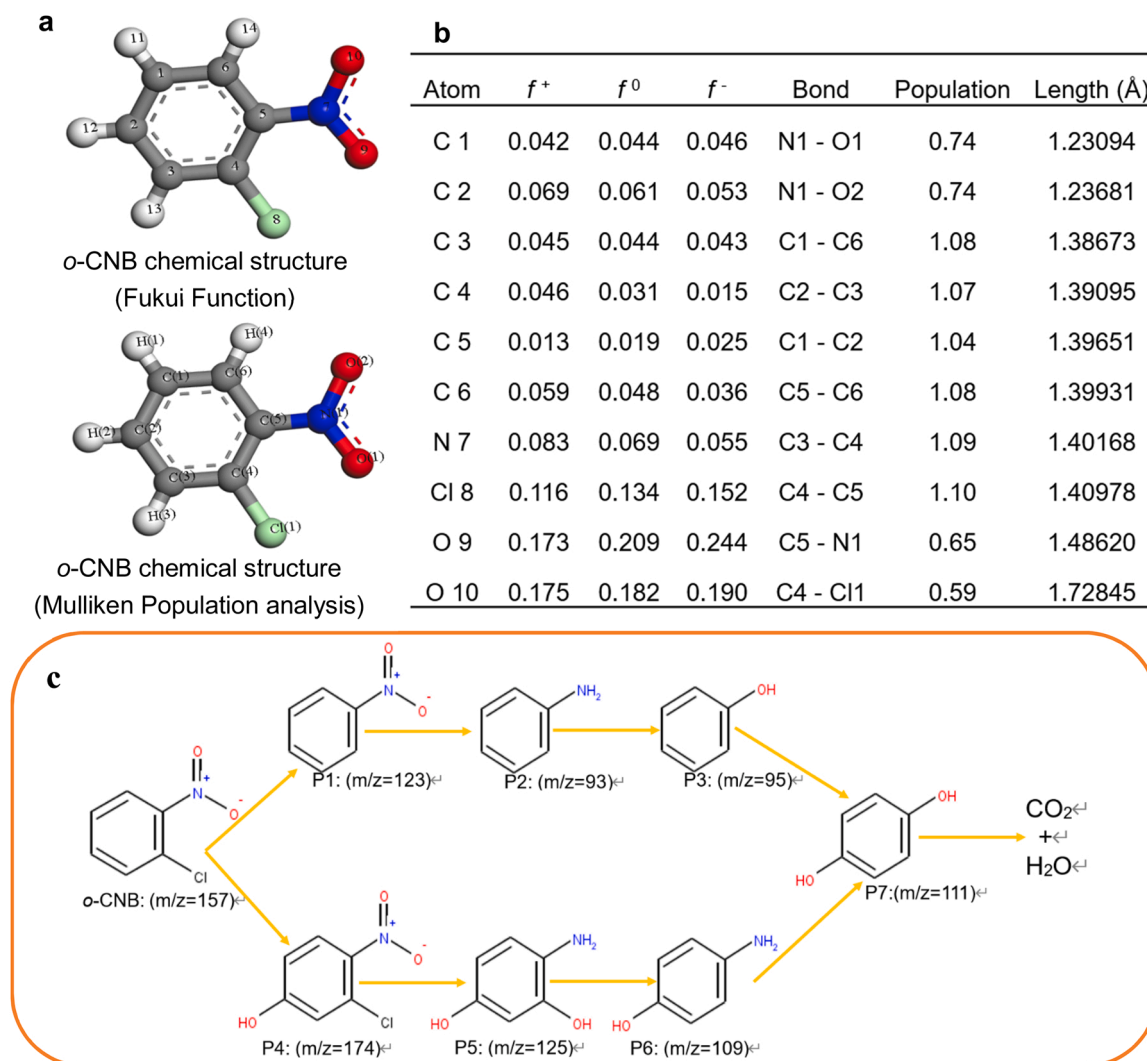


Fig. 10. *o*-CNB chemical structure (a), Fukui Function and Mulliken Population analysis (b) and proposed degradation pathway (c) of *o*-CNB in PEC system. ($[o\text{-CNB}]_0 = 0.18 \text{ mM}$, $\text{pH} = 7.0$, bias voltage = 1.5 V and $V = 50 \text{ mL}$).

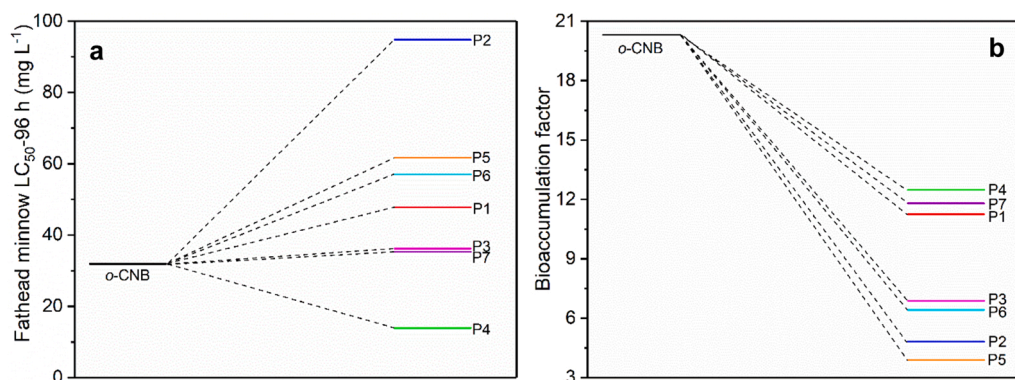


Fig. 11. The fathead minnow LC50–96 h (a) and bioaccumulation factor (b) of *o*-CNB as well as its degradation intermediates.

effectively reduced by degradation in PEC system with Au/g-C₃N₄/TNAs-0.20 photoanode.

4. Conclusions

The Au/g-C₃N₄/TNAs photoanodes were fabricated by a facile three-step procedure, including anodic oxidation, calcination and

impregnation-anneal. The results of crystalline structure, Raman analysis, surface morphology and elemental composition confirmed that g-C₃N₄ and Au nanoparticles were attached to TNAs surface. The narrow bandgap of g-C₃N₄ and the SPR effect of Au nanoparticles could effectively improve visible light absorption activity, photogenerated carrier separation, photoelectron lifetime, photoconversion efficiency and photogenerated carrier densities of TNAs photoanode. The Au/g-C₃N₄/

TNAs-0.20 possessed the best optical and photoelectrochemical properties among all photoanodes. The maximum photoconversion efficiency and photogenerated carrier densities of Au/g-C₃N₄/TNAs-0.20 photoanode were 2.39 and 12.65 times as high as that of TNAs, respectively. g-C₃N₄ and Au nanoparticles on Au/g-C₃N₄/TNAs-0.20 surface promoted the dechlorination efficiency in PEC system, which was beneficial for o-CNB degradation and TOC removal. The Au/g-C₃N₄/TNAs-0.20 photoanode exhibited good stability for the degradation of o-CNB. The bias voltage could improve the PEC performance of Au/g-C₃N₄/TNAs-0.20 photoanode for the degradation of o-CNB through promoting photogenerated carrier separation. The presence of inorganic anions and humic acid could inhibit the PEC degradation of o-CNB due to the capture of reactive species. The contribution of reactive species for the degradation of o-CNB were shown as follows: electron > •O₂⁻ > hole > •OH. The possible degradation pathway of o-CNB was inferred by GC-MS spectra and DFT calculation. The acute toxicity to fathead minnow and bioaccumulation factor of o-CNB could be effectively reduced after PEC degradation.

CRedit authorship contribution statement

Shuaishuai Xin: Investigation, Formal analysis, Writing – original draft. **Xiaoming Ma:** Investigation, Formal analysis. **Jinren Lu:** Supervision. **Guangshan Zhang:** Software, Formal analysis. **Siye Huo:** Investigation. **Mengchun Gao:** Conceptualization, Writing – review & editing, Supervision, Funding acquisition. **Peng Xu:** Software. **Wenjie Liu:** Investigation. **Wenxian Fu:** Investigation.

Declaration of Competing Interest

The authors declare that they have no known competing financial interests or personal relationships that could have appeared to influence the work reported in this paper.

Data Availability

Data will be made available on request.

Acknowledgments

The work was funded by the National Natural Science Foundation of China (No. 21878280).

Appendix A. Supplementary material

Supplementary data associated with this article can be found in the online version at [doi:10.1016/j.apcatb.2022.122174](https://doi.org/10.1016/j.apcatb.2022.122174).

References

- Z. Guo, S. Zheng, Z. Zheng, F. Jiang, W. Hu, L. Ni, Selective adsorption of p-chloronitrobenzene from aqueous mixture of p-chloronitrobenzene and o-chloronitrobenzene using HZSM-5 zeolite, *Water Res.* 39 (2005) 1174–1182, <https://doi.org/10.1016/j.watres.2004.12.031>.
- H. Wu, C. Wei, Y. Wang, Q. He, S. Liang, Degradation of o-chloronitrobenzene as the sole carbon and nitrogen sources by *Pseudomonas putida* OCNB-1, *J. Environ. Sci.* 21 (2009) 89–95, [https://doi.org/10.1016/S1001-0742\(09\)60016-4](https://doi.org/10.1016/S1001-0742(09)60016-4).
- Z. Guo, S. Zheng, Z. Zheng, Separation of p-chloronitrobenzene and o-chloronitrobenzene by selective adsorption using Silicalite-1 zeolite, *Chem. Eng. J.* 155 (2009) 654–659, <https://doi.org/10.1016/j.cej.2009.08.022>.
- X. Liang, Y. Li, G. Wei, H. He, J.W. Stucki, L. Ma, L. Pentrakova, M. Pentrak, J. Zhu, Heterogeneous reduction of 2-chloronitrobenzene by Co-substituted magnetite coupled with aqueous Fe²⁺: performance, factors, and mechanism, *ACS Earth Space Chem.* 3 (2019) 728–737, <https://doi.org/10.1021/acsearthspacechem.8b00204>.
- B. Huang, W. Qian, C. Yu, T. Wang, G. Zeng, C. Lei, Effective catalytic hydrodechlorination of o-, p- and m-chloronitrobenzene over Ni/Fe nanoparticles: effects of experimental parameter and molecule structure on the reduction kinetics and mechanisms, *Chem. Eng. J.* 306 (2016) 607–618, <https://doi.org/10.1016/j.cej.2016.07.109>.
- B. Li, J. Zhu, Removal of p-chloronitrobenzene from groundwater: effectiveness and degradation mechanism of a heterogeneous nanoparticulate zero-valent iron (NZVI)-induced Fenton process, *Chem. Eng. J.* 255 (2014) 225–232, <https://doi.org/10.1016/j.cej.2014.06.013>.
- F. Chen, S. Zeng, J. Ma, Q. Zhu, S. Zhang, Degradation of para-nitrochlorobenzene by the combination of zero-valent iron reduction and persulfate oxidation in soil, *Water Air Soil Pollut.* 229 (2018), <https://doi.org/10.1007/s11270-018-3989-5>.
- Z. Xu, Z. Sun, Y. Zhou, D. Zhang, W. Chen, Enhanced reactivity and electron selectivity of GAC-Fe-Cu ternary micro-electrolysis system toward p-chloronitrobenzene under oxic conditions, *J. Hazard. Mater.* 398 (2020), 123122, <https://doi.org/10.1016/j.jhazmat.2020.123122>.
- X. Meng, Z. Zhang, X. Li, Synergetic photoelectrocatalytic reactors for environmental remediation: a review, *J. Photochem. Photobiol. C* 24 (2015) 83–101, <https://doi.org/10.1016/j.jphotochemrev.2015.07.003>.
- Y.F. Su, G.B. Wang, D.T.F. Kuo, M.I. Chang, Y.H. Shih, Photoelectrocatalytic degradation of the antibiotic sulfamethoxazole using TiO₂/Ti photoanode, *Appl. Catal. B Environ.* 186 (2016) 184–192, <https://doi.org/10.1016/j.apcatb.2016.01.003>.
- B. Ma, S. Xin, Y. Xin, X. Ma, C. Zhang, M. Gao, F. Ma, Y. Ma, Visible-light-driven photoelectrocatalytic degradation of p-chloronitrobenzene by BiOBr/TiO₂ nanotube arrays photoelectrodes: mechanisms, degradation pathway and DFT calculation, *Sep. Purif. Technol.* 268 (2021), 118699, <https://doi.org/10.1016/j.seppur.2021.118699>.
- J. Zhang, B. Tang, G. Zhao, Selective photoelectrocatalytic removal of dimethyl phthalate on high-quality expressed molecular imprints decorated specific facet of single crystalline TiO₂ photoanode, *Appl. Catal. B Environ.* 279 (2020), 119364, <https://doi.org/10.1016/j.apcatb.2020.119364>.
- S. Fan, X. Li, J. Tan, L. Zeng, Z. Yin, M.O. Tade, S. Liu, Enhanced photoelectrocatalytic reduction dechlorinations of PCP by Ru-Pd BQDs anchored Titania NAEs composites with double Schottky junctions: First-principles evidence and experimental verifications, *Appl. Catal. B Environ.* 227 (2018) 499–511, <https://doi.org/10.1016/j.apcatb.2018.01.043>.
- C. Schnabel, M. Wörner, B. González, I. del Olmo, A.M. Braun, Photochemical characterization of p- and n-doped single crystalline silicon carbide and photoinduced reductive dehalogenation of organic pollutants at p-doped silicon carbide, *Electrochim. Acta* 47 (2001) 719–727, [https://doi.org/10.1016/S0013-4686\(01\)00752-6](https://doi.org/10.1016/S0013-4686(01)00752-6).
- Y. Ye, H. Bruning, X. Li, D. Yntema, H.H.M. Rijnaarts, Significant enhancement of micropollutant photocatalytic degradation using a TiO₂ nanotube array photoanode based photocatalytic fuel cell, *Chem. Eng. J.* 354 (2018) 553–562, <https://doi.org/10.1016/j.cej.2018.08.064>.
- R.M. Fernández-Domene, R. Sánchez-Tovar, B. Lucas-granados, M.J. Muñoz-Portero, J. García-Antón, Elimination of pesticide atrazine by photoelectrocatalysis using a photoanode based on WO₃ nanosheets, *Chem. Eng. J.* 350 (2018) 1114–1124, <https://doi.org/10.1016/j.cej.2018.06.015>.
- S.-M. Lam, J.-C. Sin, H. Zeng, H. Lin, H. Li, Z. Qin, J.W. Lim, A.R. Mohamed, Z-scheme MoO₃ anchored-hexagonal rod like ZnO/Zn photoanode for effective wastewater treatment, copper reduction accompanied with electricity production in sunlight-powered photocatalytic fuel cell, *Sep. Purif. Technol.* 265 (2021), 118495, <https://doi.org/10.1016/j.seppur.2021.118495>.
- Z. Chi, J. Zhao, Y. Zhang, H. Yu, H. Yu, Coral-like WO₃/BiVO₄ photoanode constructed via morphology and facet engineering for antibiotic wastewater detoxification and hydrogen recovery, *Chem. Eng. J.* 428 (2022), 131817, <https://doi.org/10.1016/j.cej.2021.131817>.
- B. Ma, N. Yu, S. Xin, Y. Xin, C. Zhang, X. Ma, M. Gao, Photoelectrocatalytic degradation of p-chloronitrobenzene by g-C₃N₄/TiO₂ nanotube arrays photoelectrodes under visible light irradiation, *Chemosphere* 267 (2021), 129242, <https://doi.org/10.1016/j.chemosphere.2020.129242>.
- H. Wang, Y. Liang, L. Liu, J. Hu, W. Cui, Highly ordered TiO₂ nanotube arrays wrapped with g-C₃N₄ nanoparticles for efficient charge separation and increased photoelectrocatalytic degradation of phenol, *J. Hazard. Mater.* 344 (2018) 369–380, <https://doi.org/10.1016/j.jhazmat.2017.10.044>.
- J. Wu, Y. Feng, D. Li, X. Han, J. Liu, Efficient photocatalytic CO₂ reduction by P-O linked g-C₃N₄/TiO₂-nanotubes Z-scheme composites, *Energy* 178 (2019) 168–175, <https://doi.org/10.1016/j.energy.2019.04.168>.
- Y. Tan, Z. Shu, J. Zhou, T. Li, W. Wang, Z. Zhao, One-step synthesis of nanostructured g-C₃N₄/TiO₂ composite for highly enhanced visible-light photocatalytic H₂ evolution, *Appl. Catal. B Environ.* 230 (2018) 260–268, <https://doi.org/10.1016/j.apcatb.2018.02.056>.
- Y. Jiang, Z. Sun, Q. Chen, C. Cao, Y. Zhao, W. Yang, L. Zeng, L. Huang, Fabrication of 0D/2D TiO₂ Nanodots/g-C₃N₄ S-scheme heterojunction photocatalyst for efficient photocatalytic overall water splitting, *Appl. Surf. Sci.* 571 (2022), 151287, <https://doi.org/10.1016/j.apsusc.2021.151287>.
- D. Ma, J. Wu, M. Gao, Y. Xin, T. Ma, Y. Sun, Fabrication of Z-scheme g-C₃N₄/RGO/Bi₂WO₆ photocatalyst with enhanced visible-light photocatalytic activity, *Chem. Eng. J.* 290 (2016) 136–146, <https://doi.org/10.1016/j.cej.2016.01.031>.
- Q. Zhong, H. Lan, M. Zhang, H. Zhu, M. Bu, Preparation of heterostructure g-C₃N₄/ZnO nanorods for high photocatalytic activity on different pollutants (MB, RhB, Cr (VI) and eosin), *Ceram. Int.* 46 (2020) 12192–12199, <https://doi.org/10.1016/j.ceramint.2020.01.265>.
- Y. Wang, W. Wang, J. Fu, Y. Liang, L. Yao, T. Zhu, Integrating the plasmonic sensitizer and electron relay into ZnO/Au/CdS sandwich nanotube array photoanode for efficient solar-to-hydrogen conversion with 3.2% efficiency, *Renew. Energy* 168 (2021) 647–658, <https://doi.org/10.1016/j.renene.2020.12.076>.

- [27] A. Verma, A. Srivastav, A. Banerjee, D. Sharma, S. Sharma, U.B. Singh, V. R. Satsangi, R. Shrivastav, D.K. Avasthi, S. Dass, Plasmonic layer enhanced photoelectrochemical response of Fe_2O_3 photoanodes, *J. Power Sources* 315 (2016) 152–160, <https://doi.org/10.1016/j.jpowsour.2016.03.004>.
- [28] R.B. Wei, P.Y. Kuang, H. Cheng, Y.B. Chen, J.Y. Long, M.Y. Zhang, Z.Q. Liu, Plasmon-enhanced photoelectrochemical water splitting on gold nanoparticle decorated ZnO/CdS nanotube arrays, *ACS Sustain. Chem. Eng.* 5 (2017) 4249–4257, <https://doi.org/10.1021/acsschemeng.7b00242>.
- [29] M. Sun, C. Zhai, J. Hu, M. Zhu, J. Pan, Plasmon enhanced electrocatalytic oxidation of ethanol and organic contaminants on gold/copper iodide composites under visible light irradiation, *J. Colloid Interface Sci.* 511 (2018) 110–118, <https://doi.org/10.1016/j.jcis.2017.09.103>.
- [30] Y. Yin, J. Li, Y. Wang, J. Wan, X. Du, X. Hu, E. Liu, J. Fan, Constructing ZnSe and Au co-sensitized TiO_2 nanotube arrays for high-efficiency photoelectrocatalytic activities, *Mater. Res. Bull.* 88 (2017) 33–40, <https://doi.org/10.1016/j.materresbull.2016.12.017>.
- [31] C. Wang, Y. Zhao, H. Xu, Y. Li, Y. Wei, J. Liu, Z. Zhao, Efficient Z-scheme photocatalysts of ultrathin $\text{g-C}_3\text{N}_4$ -wrapped Au/TiO_2 -nanocrystals for enhanced visible-light-driven conversion of CO_2 with H_2O , *Appl. Catal. B Environ.* 263 (2020), 118314, <https://doi.org/10.1016/j.apcatb.2019.118314>.
- [32] M.S. Nasir, G. Yang, I. Ayub, S. Wang, W. Yan, In situ decoration of $\text{g-C}_3\text{N}_4$ quantum dots on 1D branched TiO_2 loaded with plasmonic Au nanoparticles and improved the photocatalytic hydrogen evolution activity, *Appl. Surf. Sci.* 519 (2020), 146208, <https://doi.org/10.1016/j.apsusc.2020.146208>.
- [33] S. Liu, X. Jiang, G.I.N. Waterhouse, Z.M. Zhang, L.M. Yu, Efficient photoelectrocatalytic degradation of azo-dyes over polypyrrole/titanium oxide/reduced graphene oxide electrodes under visible light: performance evaluation and mechanism insights, *Chemosphere* 288 (2022), 132509, <https://doi.org/10.1016/j.chemosphere.2021.132509>.
- [34] F. Tian, Y. Zhang, J. Zhang, C. Pan, Raman spectroscopy: a new approach to measure the percentage of anatase TiO_2 exposed (001) facets, *J. Phys. Chem. C* 116 (2012) 7515–7519, <https://doi.org/10.1021/jp301256h>.
- [35] H. Rajput, R. Changotra, V. Kumar Sangal, A. Dhir, Photoelectrocatalytic treatment of recalcitrant compounds and bleach stage pulp and paper mill effluent using Au-TiO_2 nanotube electrode, *Chem. Eng. J.* 408 (2021), 127287, <https://doi.org/10.1016/j.cej.2020.127287>.
- [36] K.K. Paul, P.K. Giri, H. Sugimoto, M. Fujii, B. Choudhury, Evidence for plasmonic hot electron injection induced superior visible light photocatalysis by $\text{g-C}_3\text{N}_4$ nanosheets decorated with $\text{Ag-TiO}_2(\text{B})$ and $\text{Au-TiO}_2(\text{B})$ nanorods, *Sol. Energy Mater. Sol. Cells* 201 (2019), 110053, <https://doi.org/10.1016/j.solmat.2019.110053>.
- [37] M. Hu, Z. Xing, Y. Cao, Z. Li, X. Yan, Z. Xiu, T. Zhao, S. Yang, W. Zhou, Ti^{3+} self-doped mesoporous black $\text{TiO}_2/\text{SiO}_2/\text{g-C}_3\text{N}_4$ sheets heterojunctions as remarkable visible-light-driven photocatalysts, *Appl. Catal. B Environ.* 226 (2018) 499–508, <https://doi.org/10.1016/j.apcatb.2017.12.069>.
- [38] X. Yao, X. Hu, W. Zhang, X. Gong, X. Wang, S.C. Pillai, D.D. Dionysiou, D. Wang, Mie resonance in hollow nanoshells of ternary $\text{TiO}_2\text{-Au-CdS}$ and enhanced photocatalytic hydrogen evolution, *Appl. Catal. B Environ.* 276 (2020), 119153, <https://doi.org/10.1016/j.apcatb.2020.119153>.
- [39] M. Faisal, M.A. Rashed, J. Ahmed, M. Alsaifi, M. Jalalah, S.A. Alsareii, F. A. Harraz, Au nanoparticles decorated polypyrrole-carbon black/ $\text{g-C}_3\text{N}_4$ nanocomposite as ultrafast and efficient visible light photocatalyst, *Chemosphere* 287 (2022), 131984, <https://doi.org/10.1016/j.chemosphere.2021.131984>.
- [40] X. Ma, Q. Chen, G. Liu, Y. Zhou, D. Ma, S. Xin, C. Y, B. Zhang, Y. Xin, Construction of netlike 3D Z-scheme photoelectrodes with improved photocatalytic performance based on $\text{g-C}_3\text{N}_4$ nanosheets modified TiO_2 nanobelt-tubes, *Chem. Eng. Sci.* 226 (2020), 115844, <https://doi.org/10.1016/j.ces.2020.115844>.
- [41] L. Meng, W. Yin, S. Wang, X. Wu, J. Hou, W. Yin, K. Feng, Y.S. Ok, X. Wang, Photocatalytic behavior of biochar-modified carbon nitride with enriched visible-light reactivity, *Chemosphere* 239 (2020), 124713, <https://doi.org/10.1016/j.chemosphere.2019.124713>.
- [42] L. Li, B. Li, H. Liu, M. Li, B. Wang, Photoelectrochemical sensing of hydrogen peroxide using TiO_2 nanotube arrays decorated with RGO/CdS , *J. Alloy. Compd.* 815 (2019), 152241, <https://doi.org/10.1016/j.jallcom.2019.152241>.
- [43] Y. Cheng, J. Gao, Q. Shi, Z. Li, W. Huang, In situ electrochemical reduced Au loaded black TiO_2 nanotubes for visible light photocatalysis, *J. Alloy. Compd.* 901 (2022), 163562, <https://doi.org/10.1016/j.jallcom.2021.163562>.
- [44] S. Xin, B. Ma, G. Liu, X. Ma, C. Zhang, X. Ma, M. Gao, Y. Xin, Enhanced heterogeneous photo-Fenton-like degradation of tetracycline over $\text{CuFeO}_2/\text{biochar}$ catalyst through accelerating electron transfer under visible light, *J. Environ. Manag.* 285 (2021), 112093, <https://doi.org/10.1016/j.jenvman.2021.112093>.
- [45] X. Lin, M. Sun, Y. Yao, X. Yuan, In situ construction of N/Ti^{3+} codoped triphasic TiO_2 layer on TiO_2 nanotube arrays to improve photoelectrochemical performance, *Electrochim. Acta* 291 (2018) 319–327, <https://doi.org/10.1016/j.electacta.2018.09.099>.
- [46] F. He, B. Zhu, B. Cheng, J. Yu, W. Ho, W. Macyk, 2D/2D/0D $\text{TiO}_2/\text{C}_3\text{N}_4/\text{Ti}_3\text{C}_2\text{MXene}$ composite S-scheme photocatalyst with enhanced CO_2 reduction activity, *Appl. Catal. B Environ.* 272 (2020), 119006, <https://doi.org/10.1016/j.apcatb.2020.119006>.
- [47] Y. Xin, M. Gao, Y. Wang, D. Ma, Photoelectrocatalytic degradation of 4-nonylphenol in water with WO_3/TiO_2 nanotube array photoelectrodes, *Chem. Eng. J.* 242 (2014) 162–169, <https://doi.org/10.1016/j.cej.2013.12.068>.
- [48] P. Neta, R.E. Huie, Rate constants for reactions of nitrogen oxide (NO_3) radicals in aqueous solutions, *J. Phys. Chem. B* (1986), <https://doi.org/10.1021/j100410a035>.
- [49] G. Wang, Q. Zhang, Q. Chen, X. Ma, Y. Xin, X. Zhu, D. Ma, C. Cui, J. Zhang, Z. Xiao, Photocatalytic degradation performance and mechanism of dibutyl phthalate by graphene/ TiO_2 nanotube array photoelectrodes, *Chem. Eng. J.* 358 (2019) 1083–1090, <https://doi.org/10.1016/j.cej.2018.10.039>.
- [50] C.S. Uyguner-Demirel, N.C. Birben, M. Bekbolet, Elucidation of background organic matter matrix effect on photocatalytic treatment of contaminants using TiO_2 : a review, *Catal. Today* 284 (2017) 202–214, <https://doi.org/10.1016/j.cattod.2016.12.030>.
- [51] M. Roškaric, G. Zerjav, J. Zavašnik, A. Pintar, The influence of synthesis conditions on the visible-light triggered photocatalytic activity of $\text{g-C}_3\text{N}_4/\text{TiO}_2$ composites used in AOPs, *J. Environ. Chem. Eng.* 10 (2022), 107656, <https://doi.org/10.1016/j.jece.2022.107656>.
- [52] T. Li, P. Zhang, H. He, Z. Wang, X. Tu, D.D. Dionysiou, Highly efficient photoelectrocatalytic degradation of cefotaxime sodium on the $\text{MoSe}_2/\text{TiO}_2$ nanotubes photoanode with abundant oxygen vacancies, *J. Solid State Chem.* 303 (2021), 122455, <https://doi.org/10.1016/j.jssc.2021.122455>.
- [53] S. Xin, B. Ma, C. Zhang, X. Ma, P. Xu, G. Zhang, M. Gao, Y. Xin, Catalytic activation of peroxydisulfate by alfalfa-derived nitrogen self-doped porous carbon supported CuFeO_2 for nimesulide degradation: performance, mechanism and DFT calculation, *Appl. Catal. B Environ.* 294 (2021), 120247, <https://doi.org/10.1016/j.apcatb.2021.120247>.
- [54] Q. Wang, P. Wang, P. Xu, Y. Li, J. Duan, G. Zhang, L. Hu, X. Wang, W. Zhang, Visible-light-driven photo-Fenton reactions using $\text{Zn1-1.5xFexS/g-C}_3\text{N}_4$ photocatalyst: degradation kinetics and mechanisms analysis, *Appl. Catal. B Environ.* 266 (2020), 118653, <https://doi.org/10.1016/j.apcatb.2020.118653>.